Publications of the Astronomical Society of Australia (2021), **38**, e027, 25 pages
doi:10.1017/pasa.2021.21

CAMBRIDGE UNIVERSITY PRESS

Research Paper

Spectroscopic and photometric analysis of 21 chromospherically active variables: Activity cycles and differential rotation

O. Özdarcan

Department of Astronomy and Space Sciences, Ege University, Science Faculty, 35100 Bornova, İzmir, Turkey and TÜBİTAK National Observatory, Akdeniz University Campus, 07058 Konyaaltı, Antalya, Turkey

Abstract

We investigate magnetic activity properties of 21 stars via medium resolution optical spectra and long-term photometry. Applying synthetic spectrum fitting method, we find that all targets are cool giant or sub-giant stars possessing overall [M/H] abundances between 0 and −0.5. We find that six of these targets exhibit only linear trend in mean brightness, while eight of them clearly shows cyclic mean brightness variation. Remaining seven target appear to exhibit cyclic mean brightness variation, but this cannot be confirmed due to the long timescales of the predicted cycle compared to the current time range of the photometric data. We further determine seasonal photometric periods and compute average photometric period of each target. Analysed sample in this study provides a quantitative representation of a positive linear correlation between the inverse of the rotation period and the cycle period normalised to the rotation period, on the log-log scale. We also observe no correlation between the activity cycle length and the relative surface shear, indicating that the activity cycle must be driven by a parameter rather than the differential rotation. Our analyses show that the relative surface shear is positively correlated with the rotation period and there is a noticeable separation between main sequence stars and our sample. Compared to our sample, the relative surface shear of a main sequence star is larger for a given rotation period. However, dependence of the relative surface shear on the rotation period appears stronger for our sample. Analysis of the current photometric data indicates that the photometric properties of the observed activity cycles in eight targets seem dissimilar to the sunspot cycle.

Keywords: stars: activity – stars: late-type – stars: atmospheres

(Received 16 February 2021; revised 23 April 2021; accepted 27 April 2021)

1. Introduction

Solar irradiance measurements performed by Nimbus-7 satellite revealed that the solar constant coherently varied with daily sunspot number (Hickey et al. 1988). This result triggered the idea that the target stars observed in Mount Wilson Observatory *HK* Project (Wilson 1978; Vaughan, Preston, & Wilson 1978; Duncan et al. 1991; Baliunas et al. 1995) could exhibit variability in long-term mean brightness, like observed in their *S* indexes. Long-term Strömgren photometry in *b* and *y* bands were carried out for a sample of target stars of the *HK* project and a correlation was found between chromospheric and photometric variations, but with a clear diversity between younger and older stars (Lockwood, Skiff, & Radick 1997, Radick et al. 1998). Since the main reference is the Sun itself, almost all target stars were chosen as main sequence stars from different spectral types. Baliunas et al. (1996) used a sample from *HK* project targets and discovered a correlation between the cycle length normalised to the rotation period ($P_{\rm cyc}/P_{\rm rot}$) and the dynamo number, $D \sim 1/P_{\rm rot}$, which was expected to provide clues about the type of the dynamo operating in these stars. Further studies on the *HK* project targets also revealed a linear positive correlation between $P_{\rm rot}$ and the rotational period variation amplitude ΔP (Donahue, Saar, & Baliunas 1996). Since ΔP is commonly accepted as the proxy of the surface differential rotation, the correlation indicates that slow rotators possess stronger surface differential rotation compared to fast rotators.

In addition to the Strömgren photometry, some other projects on the long-term photometric observations of chromospherically active stars from various luminosity classes have started by different groups (Henry & Eaton 1995; Strassmeier et al. 1997; Rodonò et al. 2001) with automated photoelectric telescopes (APTs). These efforts enabled to trace long-term photometric behaviour of chromospherically active giant and subgiant stars, in addition to the *HK* project stars.

Efficient and precise broad-band *V* observations obtained from APTs allowed studying photometric activity cycles for main sequence and giant stars (Oláh & Strassmeier 2002; Messina & Guinan 2003; Oláh et al. 2013). Furthermore, these observations enabled studies on photometric period variations and long-term tracing of the light curve properties of giant and subgiant stars (Jetsu, Henry, & Lehtinen 2017). These studies allowed to make a comparison between photometric properties of the magnetic activity on these stars and the sunspot cycle (see, e.g. Fekel & Henry 2005; Özdarcan et al. 2010). For instance, Fekel et al. (2002) analysed long-term photometric data of two SB1 systems, HD 89546 and HD 113816, and did not find any correlation between the photometric period and the mean brightness, which is a typical properties of the sunspot cycle. However, 10 yr later, Özdarcan,

Author for correspondence: O. Özdarcan, E-mail: orkun.ozdarcan@ege.edu.tr
Cite this article: Özdarcan O. (2021) Spectroscopic and photometric analysis of 21 chromospherically active variables: Activity cycles and differential rotation. *Publications of the Astronomical Society of Australia* **38**, e027, 1–25. https://doi.org/10.1017/pasa.2021.21

Table 1. Identifiers, J2000 equatorial coordinates, *V* magnitudes, and the rotation periods (*P*) of the the target stars. In the last column, the first reference is for *V* magnitude and the second reference is for the period.

Identifier	RA (J2000)	Dec (J2000)	*V*	*P*	Ref.
	(h m s)	(°′″)	(mag)	(day)	
V660 Vir	14 22 50	+06 41 12	11.69	70.8	Zacharias et al. (2013), Schirmer, Bernhard, & Lloyd (2009)
DG Ari	02 55 21	+15 39 51	11.15	33.998	Høg et al. (2000), Lloyd et al. (2011)
V1263 Tau	03 24 06	+07 29 27	10.61	20.504	Schmidt et al. (2009), Bernhard & Lloyd (2008b)
FK CMi	07 36 42	+03 54 20	11.22	19.28	Schmidt et al. (2009), Bernhard & Otero (2011)
V383 Vir	12 16 53	+05 41 26	10.20	14.26	Schmidt et al. (2009), Berdnikov & Pastukhova (2008)
BD+04 3503	17 46 25	+03 58 49	9.54	8.447	Kiraga (2012), Bernhard & Otero (2011)
BD+02 3610	18 32 19	+02 14 54	11.55	12.84	Kiraga (2012), Bernhard & Otero (2011)
GH Psc	00 57 08	+10 25 57	10.05	34.81	Schmidt et al. (2009), Bernhard (2008)
TYC 723-863-1	05 48 23	+12 18 26	10.40	44.85	Høg et al. (2000), Schirmer et al. (2009)
HD 354410	19 57 53	+14 20 18	11.20	27.573	Kiraga (2012), Lloyd et al. (2011)
TYC 1094-792-1	20 55 51	+10 23 41	11.46	10.15	Høg et al. (2000), Bernhard & Lloyd (2008d)
UY Equ	21 10 54	+08 58 16	11.58	14.06	Schmidt et al. (2009), Bernhard & Lloyd (2008d)
FP Psc	00 43 49	+18 46 53	10.91	13.74	Høg et al. (2000), Bernhard & Lloyd (2008d)
TYC 1541-191-1	17 24 05	+18 29 37	11.23	11.563	Høg et al. (2000), Bernhard & Lloyd (2008a)
V343 Del	21 03 23	+19 30 56	10.50	10.377	Schmidt et al. (2009), Lloyd et al. (2011)
V439 Peg	21 30 41	+22 01 43	10.55	24.135	Høg et al. (2000), Bernhard & Lloyd (2008c)
TYC 1683-144-1	21 59 45	+16 57 38	11.27	44.22	Høg et al. (2000), Schirmer et al. (2009)
BE Ari	01 47 10	+23 45 32	10.08	21.203	Høg et al. (2000), Bernhard & Lloyd (2008b)
V592 Peg	23 21 53	+23 16 56	10.79	19.09	Zacharias et al. (2013), Lloyd et al. (2011)
TYC 4667-90-1	00 15 08	−03 20 00	11.24	8.84	Høg et al. (2000), Bernhard & Otero (2011)
BC Sex	10 30 03	−00 47 32	11.79	15.37	Schmidt et al. (2009), Berdnikov & Pastukhova (2008)

Evren, & Henry (2012) re-analysed the long-term photometry of HD 89546, which was doubled as the time coverage of the data compared to the former study and showed that the distribution of the mean brightness with respect to the photometric period is similar to the one observed in the sunspot cycle (see Figure 6 in their study). Besides these APT observations, photometric sky surveys, such as The All Sky Automated Survey (ASAS3, Pojmanski 1997; 2002; Pojmanski, Pilecki, & Szczygiel 2005) and All-Sky Automated Survey for Supernovae Sky Patrol (ASAS-SN, Shappee et al. 2014; Kochanek et al. 2017) also provided long-term photometric data for a given position on the sky plane, which is also useful for long-term photometric analyses of chromospherically active stars (see, e.g. Özdarcan & Dal 2018). All these studies led to an increase in the number of well-studied giant and subgiant stars, thus reliable statistical evaluation of magnetic activity properties of these stars became possible. Owing to these studies, it came out that both main sequence and giant stars obey the relation between $(P_{\rm cyc}/P_{\rm rot})$ and $(1/P_{\rm rot})$, without a significant diversity between the luminosity classes (Oláh & Strassmeier 2002; Oláh et al. 2009). However, giant and subgiant stars still need more attention. We still do not know precisely if the photometric properties of the magnetic activity in these stars are similar or dissimilar to the photometric properties of the solar activity. On the other hand, test bench of the theoretical studies, in the scope of the mean field dynamo models, has not been fulfilled sufficiently for cool giant and subgiant region in the Hertzsprung–Russell diagram.

In this study, we present analyses of spectroscopic and long-term photometric observations of 21 stars, which are listed in Table 1 along with their basic properties. These stars were suggested as candidate RS CVn variables in the studies listed in the table. We give technical details of the spectroscopic observations and data reductions in the next section. Then, we focus on spectral types, spectral features in terms of chromospheric activity, and global atmospheric properties of the target stars. In Section 3, we describe sources of the photometric data and analyse long-term brightness variation, together with seasonal light curves. We investigate possible relations between the activity cycle length, the rotation period, and the relative surface shear (i.e. the surface differential rotation) in Section 4. We summarise and discuss our findings in the last section.

2. Spectroscopy

2.1. Data

We obtained intermediate resolution optical échelle spectra of the target stars at TÜBİTAK National Observatory (TNO) with 1.5-m Russian-Turkish telescope and Turkish Faint Object Spectrograph Camera (TFOSC[1]). Until 2017 August 8, optical spectra were recorded by a back illuminated CCD camera with 15 × 15 μm^2 pixel size and 2 048 × 2 048 pixels. After that date, CCD camera was replaced by a new Andor DW436-BV 2 048 × 2 048 pixels

[1] https://tug.tubitak.gov.tr/en/teleskoplar/rtt150-telescope-0.

https://doi.org/10.1017/pasa.2021.21 Published online by Cambridge University Press

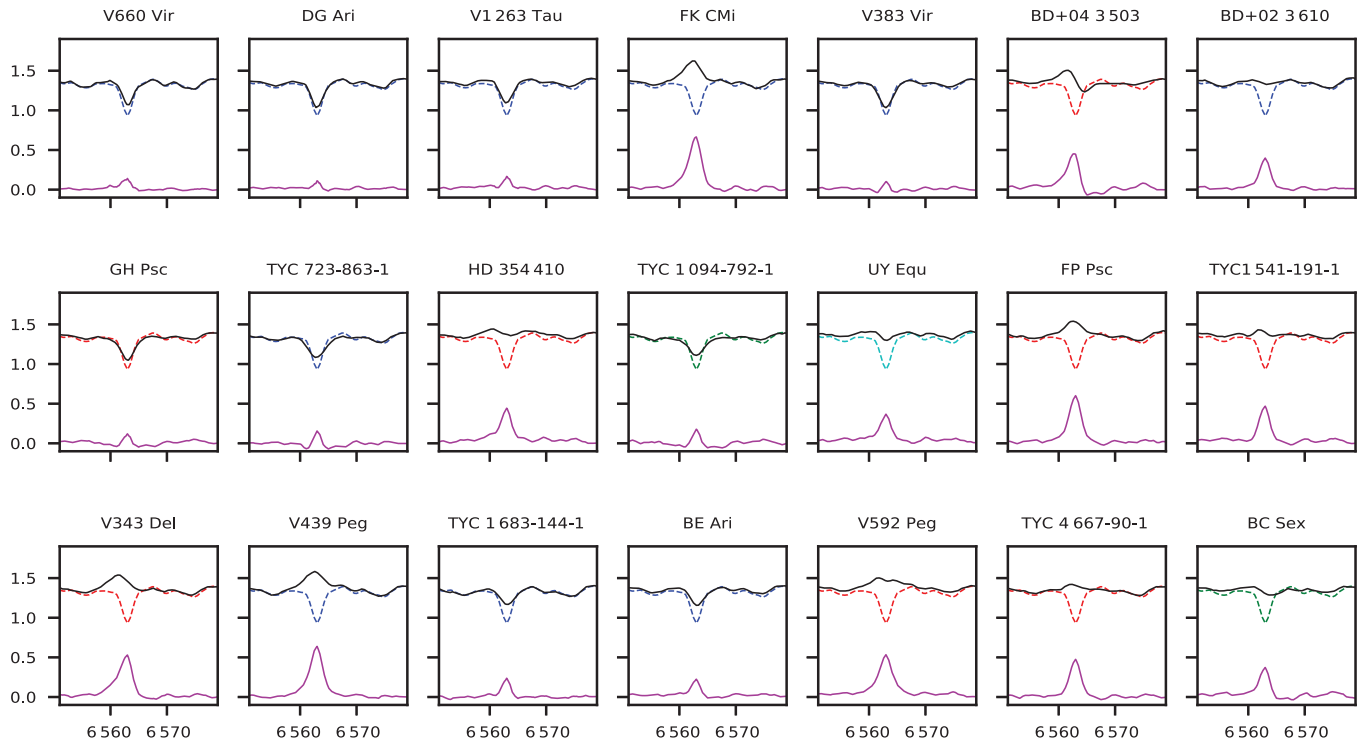

Figure 1. H_α line profiles of the target stars (black lines), comparison stars (dashed lines), and the difference spectrum in the sense of target-minus-comparison (magenta lines). Horizontal and vertical axes show wavelength (Å) and normalised flux, respectively. We shift line profiles of the target and comparison stars upwards by 0.4 in order to see difference spectrum separately. The spectra of comparison stars κ Oph, 35 Peg, *o* Psc, and ϵ Psc are in blue, red, green, and cyan colours, respectively.

CCD camera with a pixel size of $13.5 \times 13.5\ \mu m^2$. This instrumental set-up enabled us to record optical spectrum between 3 900 and 9 100 Å in 11 échelle orders with actual spectral resolution ($R = \lambda/\Delta\lambda$) of $2\,700 \pm 500$ around $\lambda = 5\,500$ Å for both CCD cameras.

Raw object spectra were reduced by following conventional échelle reduction steps, starting with bias correction and followed by flat-field division by bias-corrected and normalised flat-field image, scattered light correction, cosmic rays removal, and extraction of the spectra from the échelle orders. Wavelength calibration of the object spectra were done by Fe-Ar calibration lamp spectra. In the final step, extracted and wavelength calibrated object spectra were normalised to the unity order by order, using fourth or fifth order cubic spline functions. All these steps were carried out under IRAF environment.[2] Since normalisation of spectra is based on fitting a mathematical function to a stellar spectrum, we use these normalised spectra as the initial input for atmosphere analysis. During the atmosphere analysis, these spectra are re-normalised with respect to a proper template synthetic spectrum, which is more reliable for spectrum normalisation.

2.2. Spectral types and features

Beside target stars, we obtained optical échelle spectra of four more stars, κ Oph (K2 III, Gray et al. 2003), 35 Peg (K0 III, Frasca et al. 2009), *o* Psc (G8 III, Jofré et al. 2015), and ϵ Psc (G9 III, Soubiran et al. 2008) with the same instrumental set-up, which are to be used as observational comparison templates. Comparing the template spectra with each of target star spectrum individually, we see that each of the target star spectrum nicely match one of the comparison template spectra, meaning that our sample include only giant and subgiant stars. In Figures 1 and 2, we show H_α and Ca II H& K line profiles of each target star and the best-matched observational comparison spectrum. These spectral lines are very sensitive to the chromospheric activity observed in cool stars. Some of our target stars exhibit direct emission in H_α line profile, while emission features become visible for other stars in the difference spectrum, in the sense of target-minus-comparison. Emission features are more pronounced in Ca II H& K line profiles. These line profiles strongly indicate chromospheric activity on these targets. Among our sample, V439 Peg exhibits the strongest emission features both in H_α and Ca II H& K lines and appears as the most active star in the sample. Another noticeable feature can be seen in H_α line profile of BD+04 3503, which resembles P Cyg line profile. Since the spectral features strongly indicate chromospheric activity, we may speculate that it might be a spectroscopic binary candidate, that one component might be very active and show emission in H_α, while secondary component is a less active or inactive star, thus contributing to composite H_α line profile in form of absorption. Since we only have a single spectrum per target and resolution of TFOSC spectra is limited, it is not possible to detect any shift in spectral lines as an evidence of orbital motion or any spectral line of a possible secondary component.

2.3. Atmosphere analysis

For further detailed atmospheric analysis of the target stars, we adopt synthetic spectrum fitting method. Main idea of the method is to minimise the difference between the observed and the synthesised spectra for defined wavelength ranges. We apply the method

[2]The Image Reduction and Analysis Facility is hosted by the National Optical Astronomy Observatories in Tucson, Arizona at URL iraf.noao.edu.

https://doi.org/10.1017/pasa.2021.21 Published online by Cambridge University Press

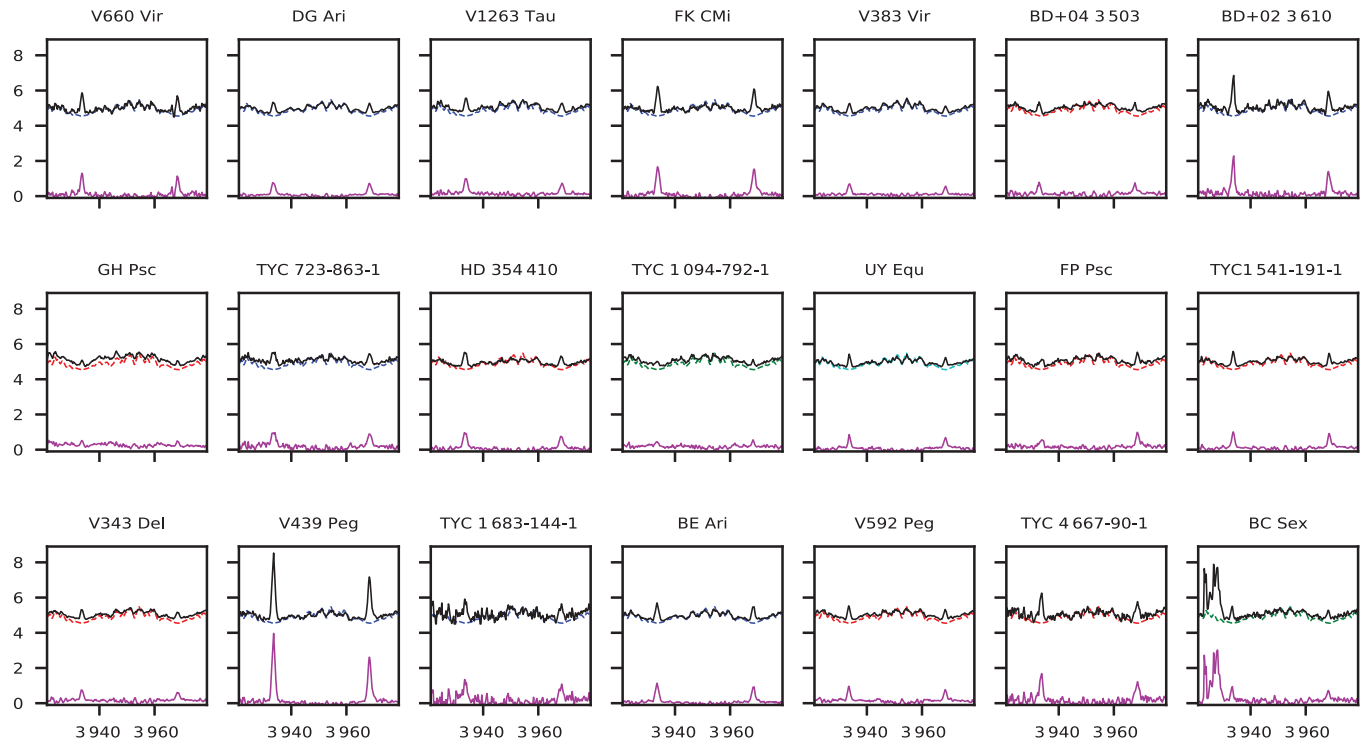

Figure 2. Same as Figure 1 but for Ca II H& K line profiles. Due to the very strong emission in V439 Peg spectrum, we shift all observed spectra upwards by 4.5, so that emission strength can be seen separately. Note that emission-like feature around 3 925 Å seen in the spectrum of BC Sex is a very strong cosmic spike, which could not be removed properly. However, emission feature of Ca II K line profile is still visible next to the spike.

by the newest version of ISPEC software (Blanco-Cuaresma et al. 2014), which includes various radiative transfer codes, line lists, and model atmospheres in a python framework with a user-friendly graphical user interface. Since each target star appears as a cool giant or subgiant star, we use TURBOSPECTRUM (Alvarez & Plez 1998; Plez 2012) radiative transfer code in conjunction with MARCS model atmospheres (Gustafsson et al. 2008). These models are one-dimensional hydrostatic plane-parallel and spherical models computed under local thermodynamic equilibrium (LTE) assumption. In synthetic spectrum fitting and computing, we adopt spherical models, which are more proper for giant stars due to their large radii. Line list compiled from Vienna Atomic Line Database (VALD3, Ryabchikova et al. 2015) provided by ISPEC software is adopted for spectrum synthesising.

For each target star, the first step is to adopt a set of atmospheric parameters estimated in spectrum comparison described in the previous section and synthesise a template spectrum. Then, we shift observed spectrum of the target star to the rest wavelength and re-normalise it with respect to the template. In the normalisation, we adopt the wavelength region between 3 900 and 6 800 Å and compute median for every 5 Å bin within this range for the template spectrum. Computed median values within this wavelength range form a function, which we adopt as the continuum function. Then we divide object spectrum by the continuum function and obtain normalised spectrum of the object. Shifted and re-normalised target spectrum is our input observed data. We set the effective temperature ($T_{\rm eff}$), logarithm of the surface gravity (log$g$), metallicity [(M/H)], micro-turbulence velocity ($v_{\rm mic}$), and spectral resolution as adjustable parameters during synthetic spectrum fitting. Considering resolution of TFOSC spectra and reported rotation periods of target stars in Table 1, we neglect line broadening due to projected rotational velocity (v sin i) and macro-turbulence velocity, that is, fix them to zero. We adopt wavelength range between 4 900 and 6 800 Å for synthetic spectrum fitting but avoid highly blended absorption lines, very strong and broad spectral lines, such as H_α and NaI D resonant lines. We did not extend wavelength range towards bluer part of the spectra since flux of target stars steeply decreases at these wavelengths, leading to considerably lower signal-to-noise ratio. This is natural indication of that we are dealing with cool and red stars. Beyond the 6 800 Å, telluric lines and bands are dominant structures thus we omit this part of the spectrum in atmosphere analysis. When fitting process converges to a solution, we synthesise final template spectrum by adopting solution parameters. Since resolution of TFOSC spectra is not high, it was not necessary to repeat this process iteratively, that is, applying this procedure only for once is fairly enough to achieve an acceptable fit to the observed spectrum and reasonable atmospheric parameters. We tabulate synthetic spectrum fitting results in Table 2.

We show observed spectrum of each target with its best-fitting synthetic spectrum in the appendix (Figure A.1). It can be noticed that the spectral lines of BD+04 3503 are shallower and broader compared to the other target stars with similar atmospheric parameters. Furthermore, resulting spectral resolution for this star is considerably lower than the others. These results, together with spectral features of this star reported in Section 2.2, support our speculation on spectroscopic binary possibility. For this star, we repeat synthetic spectrum fitting process with including v sin i as additional adjustable parameters, or neglecting rotational broadening and fixing resolution to different values

https://doi.org/10.1017/pasa.2021.21 Published online by Cambridge University Press

Table 2. Atmospheric analysis results of target stars. In the last two columns, resolution ($R = \lambda/\Delta\lambda$) and estimated spectral types of the target stars are given. Spectral type estimation is done by comparing final atmospheric parameters with calibration given in Gray (2005).

Target	Comparison	HJD	Exp. (s)	SNR	$T_{\rm eff}$ (K)	log*g* (cgs)	[M/H]	v_{mic} (km s^{-1})	*R*	Sp
V660 Vir	κ Oph	2 458 227.4379	3 600	97	4 468±136	2.59±0.30	0.02±0.15	1.78±0.32	3 411±227	K3 III
DG Ari	κ Oph	2 457 671.5264	3 600	210	4 444±157	2.37±0.44	−0.02±0.17	1.72±0.34	2 757±200	K3 III
V1263 Tau	κ Oph	2 457 997.5884	2 700	147	4 426±217	2.14±0.42	−0.53±0.23	1.56±0.41	2 768±241	K3 III
FK CMi	κ Oph	2 458 194.2858	3 600	85	4 497±168	2.67±0.51	−0.49±0.19	1.86±0.46	2 740±231	K2 III
V383 Vir	κ Oph	2 458 227.3942	3 600	225	4 655±206	2.62±0.45	0.05±0.19	1.56±0.37	2 611±207	K1 III
BD+04 3503	35 Peg	2 458 394.2246	2 400	205	4 858±304	3.11±0.59	−0.05±0.25	1.26±0.55	1 648±183	K0 III-IV
BD+02 3610	κ Oph	2 458 394.3054	3 600	131	4 489±128	3.02±0.30	0.00±0.14	1.93±0.41	2 474±183	K2 III-IV
GH Psc	35 Peg	2 458 345.4909	2 400	178	4 866±278	2.78±0.53	−0.05±0.24	1.34±0.41	2 828±251	K0 III
TYC 723-863-1	κ Oph	2 458 194.2365	2 700	123	4 414±166	2.11±0.56	−0.10±0.19	1.84±0.35	2 323±180	K3 III
HD 354410	35 Peg	2 458 227.5840	3 600	119	4 729±273	2.76±0.57	−0.47±0.25	2.05±0.53	2 235±216	K1 III
TYC 1094-792-1	*o* Psc	2 458 265.5389	3 000	89	5 240±399	3.59±0.53	−0.49±0.29	1.74±0.70	2 999±329	G4 III-IV
UY Equ	ϵ Psc	2 458 346.3991	3 600	123	4 706±216	2.98±0.54	−0.54±0.20	1.71±0.48	3 367±295	K1 III
FP Psc	35 Peg	2 458 395.5739	3 600	147	4 662±253	2.65±0.48	−0.50±0.24	1.69±0.47	2 841±259	K1 III
TYC 1541-191-1	35 Peg	2 458 226.5153	3 600	123	4 705±225	2.94±0.75	−0.53±0.22	1.55±0.53	2 783±266	K1 III
V343 Del	35 Peg	2 458 265.5785	2 400	92	4 629±214	2.86±0.59	−0.36±0.21	1.77±0.47	2 599±226	K1 III
V439 Peg	κ Oph	2 458 395.3852	3 000	135	4 363±145	2.32±0.42	−0.10±0.16	1.90±0.35	2 614±189	K3 III
TYC 1683-144-1	κ Oph	2 458 395.4778	3 600	100	4 456±141	2.49±0.39	−0.03±0.15	1.92±0.35	2 582±188	K3 III
BE Ari	κ Oph	2 458 345.5277	2 400	170	4 433±182	2.23±0.37	−0.02±0.19	1.58±0.34	2 625±197	K3 III
V592 Peg	35 Peg	2 458 345.4500	3 600	134	4 741±243	2.60±0.56	−0.19±0.22	1.49±0.40	2 902±250	K1 III
TYC 4667-90-1	35 Peg	2 458 395.5278	3 600	113	4 614±178	2.70±0.52	0.02±0.17	1.60±0.40	2 259±188	K1 III
BC Sex	*o* Psc	2 458 227.3453	3 600	101	4 947±331	3.32±0.85	−0.54±0.28	1.56±0.64	2 575±274	G9 III-IV

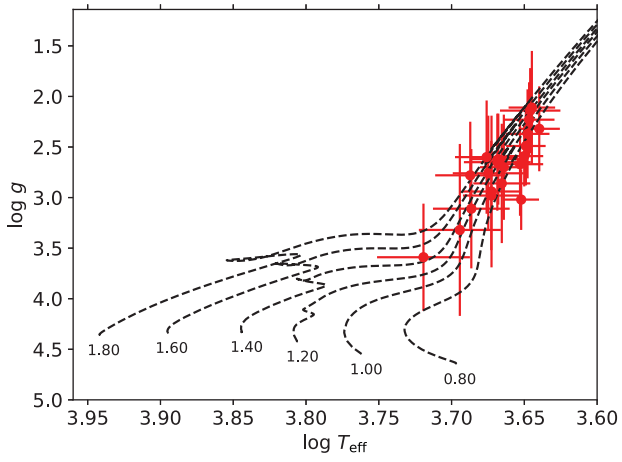

Figure 3. Positions of the target stars on log T_{eff} − log *g* plane. Evolutionary tracks are from Bressan et al. (2012) for $Z = 0.014$ and $Y = 0.273$. We also show corresponding mass of each track in unit of the solar mass.

between 2 200 and 3 300. All these tests result in slightly different atmospheric parameters which basically agree within the uncertainties given in Table 2. We show positions of the target stars on log $T_{\rm eff}$ − log *g* plane in Figure 3, which clearly shows that our targets are located in giant and subgiant regions in the plane.

3. Photometry

Long-term *V*-band photometry of each target star was extracted from The All Sky Automated Survey (ASAS, Pojmanski 1997; Pojmanski 2002; Pojmanski et al. 2005) and All-Sky Automated Survey for Supernovae Sky Patrol (ASAS-SN, Shappee et al. 2014; Kochanek et al. 2017) databases. Compiled photometric data from these databases provide observational time base of 16–18 yr, depending on the target. There is a 3- or 4-yr time gap between the last observation of ASAS and the first observation of ASAS-SN data. This gap was filled by ASAS-3N data (Pojmański 2021), which enables us to have continuous *V*-band photometry of each target without considerable data gap. There are time ranges where data overlap occurs between ASAS and ASAS-3N data. Similar overlap exists for ASAS-3N and ASAS-SN data. These overlaps provide an advantage of comparing different datasets and check for any systematic shift in magnitude axis. ASAS and ASAS-3N data mostly agree, but considerable shifts (maximum $0\overset{m}{.}2$) of ASAS-SN data with respect to the ASAS and ASAS-3N data were observed. In such cases, we adopt ASAS data as the reference dataset and apply constant shift in magnitudes with respect to the ASAS data. We do not expect any major effect in cycle search and photometric period analysis results due to such shifts, since we only remove systematic offsets by comparing overlapped data of different datasets.

Before starting analysis, we plot compiled data against time and check for highly deviated observations with respect to the general trend of the whole light curve. The data are mainly used to investigate long-term brightness variation and seasonal photometric behaviour. Therefore, any highly deviated data point, regardless if it shows an instantaneous brightness variation (e.g. flare) or not, were discarded from the dataset. We further check outlier data points in by inspecting phase-folded seasonal light curves. For each seasonal light curve possessing sufficient data points and

https://doi.org/10.1017/pasa.2021.21 Published online by Cambridge University Press

Table 3. Cycle period *P* and amplitude *A* found in Lomb-Scargle periodogram. In the last column, Δt is the time span of the compiled photometric data.

Target	*P* (year)	*A* (mmag)	Δt (year)
V660 Vir	7.9±0.2	38±4	16
FK CMi	11.3±0.1	152±5	18
V383 Vir	11.0±0.3	43±3	16.5
BD+04 3503	8.3±0.3	30±3	17.6
BD+02 3610	8.0±0.3	48±6	17
UY Equ	10.0±0.4	34±4	16
FP Psc	6.8±0.1	36±2	15
TYC 4667-90-1	4.8±0.8	37±4	18

considerable light curve amplitude, we find a photometric period (see Section 3.2) and compute phase-folded light curve with respect to that period. In order to detect outliers, we fit a cubic spline to the phase-folded light curve, compute residuals from the best-fitting cubic spline and their mean absolute deviation (σ). If any data point is out of $\pm 3\sigma$ band of the residuals, it is removed from the data. Repeating this procedure iteratively until there is no outlier in the corresponding light curve, we obtain final light curves for photometric analysis.

3.1. Mean brightness variations

In the first step of the photometric analysis, we inspect long-term mean brightness variation of each target. For a given target, we first apply linear fit to all data in order to remove any sign of a possible very long-term variation with a timescale much longer than the time base of current photometric data. Then we obtain residuals from the linear fit (hereafter, linear residuals), which scatters around zero level, and search for any long-term periodicities in the linear residuals via Lomb–Scargle periodogram (Lomb 1976; Scargle 1982). Inspecting compiled photometry of target stars given in Figure 4, we did not expect any cyclic variation timescale shorter than 1 year. In order to avoid rotational modulation signal and its harmonics, which could suppress cycle signal in the amplitude spectrum, we did not include periods shorter than 100 d in cycle search. Thus, we scan period range between 100 d and the time span of the compiled photometric data (Δt) given in the last column of the Table 3. We find that 8 of 21 target stars show cyclic mean brightness variation with one significant period. We present compiled photometric data of all target stars and detected mean brightness variations for eight stars in Figure 4 and tabulate detected cyclic variation periods in Table 3. Among remaining 13 targets, 6 of them, DG Ari, V1263 Tau, HD 354410, TYC 1541-191-1, V343 Del, and V592 Peg, only exhibit linear increase or decrease in mean brightness. For the each of remaining seven targets, GH Psc, TYC 723-863-1, TYC 1094-792-1, BC Sex, BE Ari, V439 Peg, and TYC 1683-144-1, we still find statistically significant cycles signal above 3σ threshold, but resulting cycles do not repeat itself more than 1.5 times in the current dataset. Further observations are needed to check the reliability of the detected signals; therefore, we did not consider these stars as cyclic variables and did not include them in Table 3.

We also provide amplitude spectra of the Lomb–Scargle periodogram in Figure B.1, where one may see two peaks above 3σ threshold for some of the target stars. However, these secondary peaks hardly exceed 3σ threshold or vanish below that level after prewhitening of the primary period, therefore did not considered as significant signal.

3.2. Analysis of seasonal light curves

After analysing global brightness variation, we focus on analysis of seasonal light curves of each target. For each seasonal light curve, we try to find photometric period and peak-to-peak light curve amplitude. Inspecting seasonal light curves, we see that light curve shapes are asymmetric or double-humped, which is a typical light curve feature of a chromospherically active star.

Such light curves can be fitted satisfactorily by combining a number of signals with different periods, amplitudes, and phases. One of these signals is the main signal and the remaining signals have periods which are harmonics of the period of the main signal. In this case, one may find many periods, which are statistically significant, for a given single light curve. Our aim is neither make a perfect trigonometric fit to a light curve nor to study harmonics of the main period, but to find a unique period, which represents the light curve as good as possible. Therefore, we adopt ANOVA method (Schwarzenberg-Czerny 1996) which combines strengths of Fourier method and ANOVA statistics. ANOVA method is capable to detect a unique period for an asymmetric or double-humped light curve by evaluating scatter of the phase-folded observational data with respect to a set of trial periods. This method is also very efficient in peak detection and damping alias periods.

We carry out analysis of each target by using the residuals obtained from the linear fit in Section 3.1. The purpose of using the residuals is to reduce unwanted effects of any global (linear) brightening or dimming trend on period and peak-to-peak amplitude detection from seasonal light curves. For each season of each target, we determine start, end, and mean HJD values together with photometric period and its statistical uncertainty, maximum, minimum, and mean brightnesses, peak-to-peak light curve amplitude and number of data points in the season. We tabulate numerical values of these parameters in Table C.1. We adopt the method proposed by Schwarzenberg-Czerny (1991) to estimate the uncertainty of the seasonal photometric periods. We also compute rotation period of each target by averaging corresponding seasonal photometric periods tabulated in Table C.1. Standard deviation of seasonal photometric periods of each target is adopted as the uncertainty of computed rotation period. Computed rotation periods and uncertainties are listed at the end of Table C.1. Comparing computed rotation periods with the previously reported periods given in Table 1, we see that the computed periods in this study agrees with the previously reported periods in 1σ error bar, except FK CMi and FP Psc. However, for these two stars, difference between previously reported periods and computed periods in this study slightly exceed 1σ error bar.

In the context of solar–stellar connection, one may expect to observe relations between mean brightness, peak-to-peak light curve amplitude, and photometric period. In the Sun, when a new sunspot cycle begins, small sunspots appear at higher latitudes which rotate slower than the solar equator, hence these sunspots have longer rotation periods and causes low-amplitude light loss due to their small size. At the middle of the cycle, sunspots mostly emerge at mid-latitudes with a larger areas and shorter rotation periods compared to the beginning of the cycle. At the end of the cycle, sunspots emerge at lower latitudes with smaller areas and

https://doi.org/10.1017/pasa.2021.21 Published online by Cambridge University Press

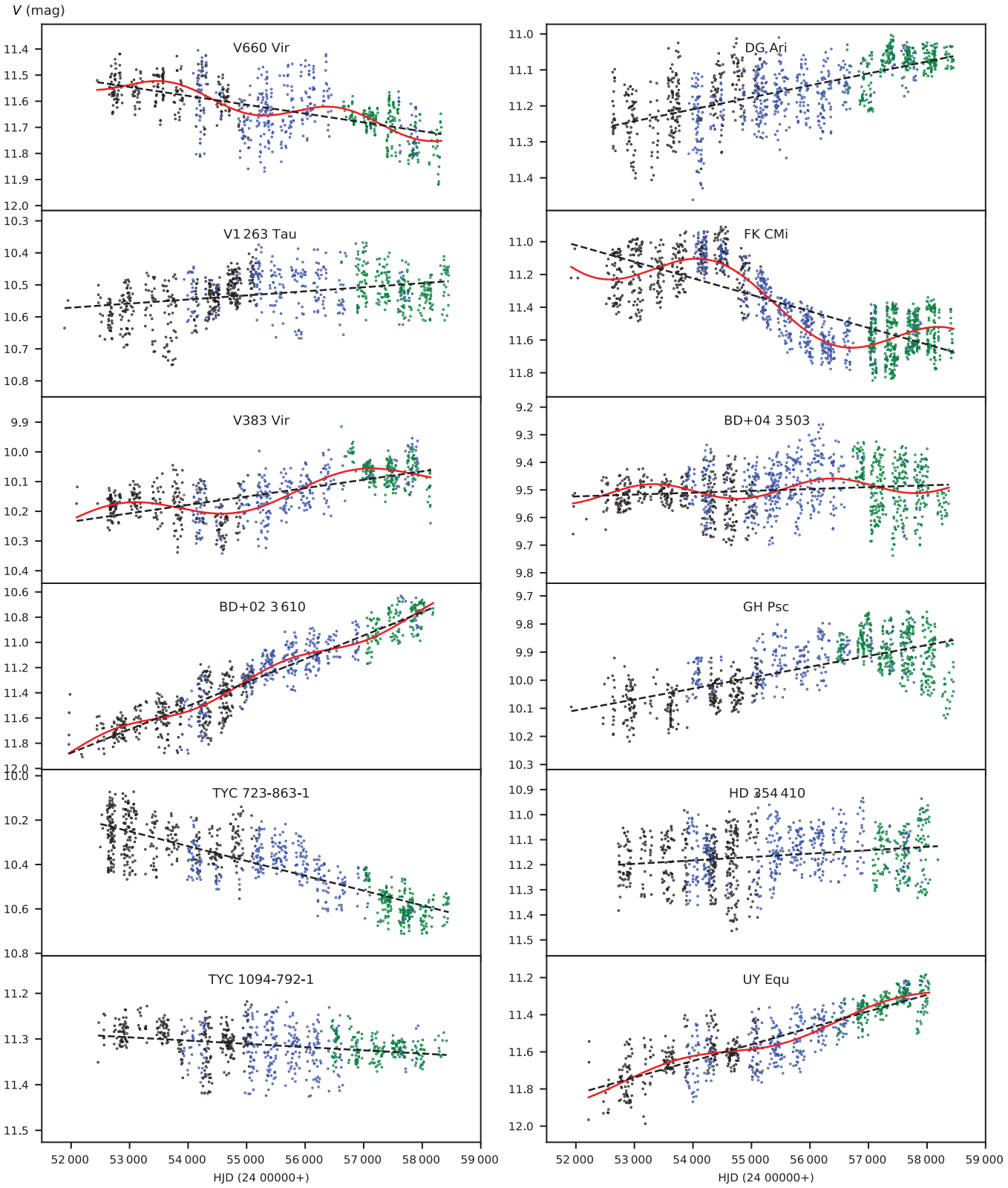

Figure 4. Compiled long-term *V*-band photometric data of target stars. Black, blue, and green points denote ASAS, ASAS-3N, and ASAS-SN data, respectively. For each star, dashed line shows linear fit to the data. If the target possesses a significant periodic signal, then the signal is shown with continuous (red) curve, which is the combination of periodic signal and linear fit.

https://doi.org/10.1017/pasa.2021.21 Published online by Cambridge University Press

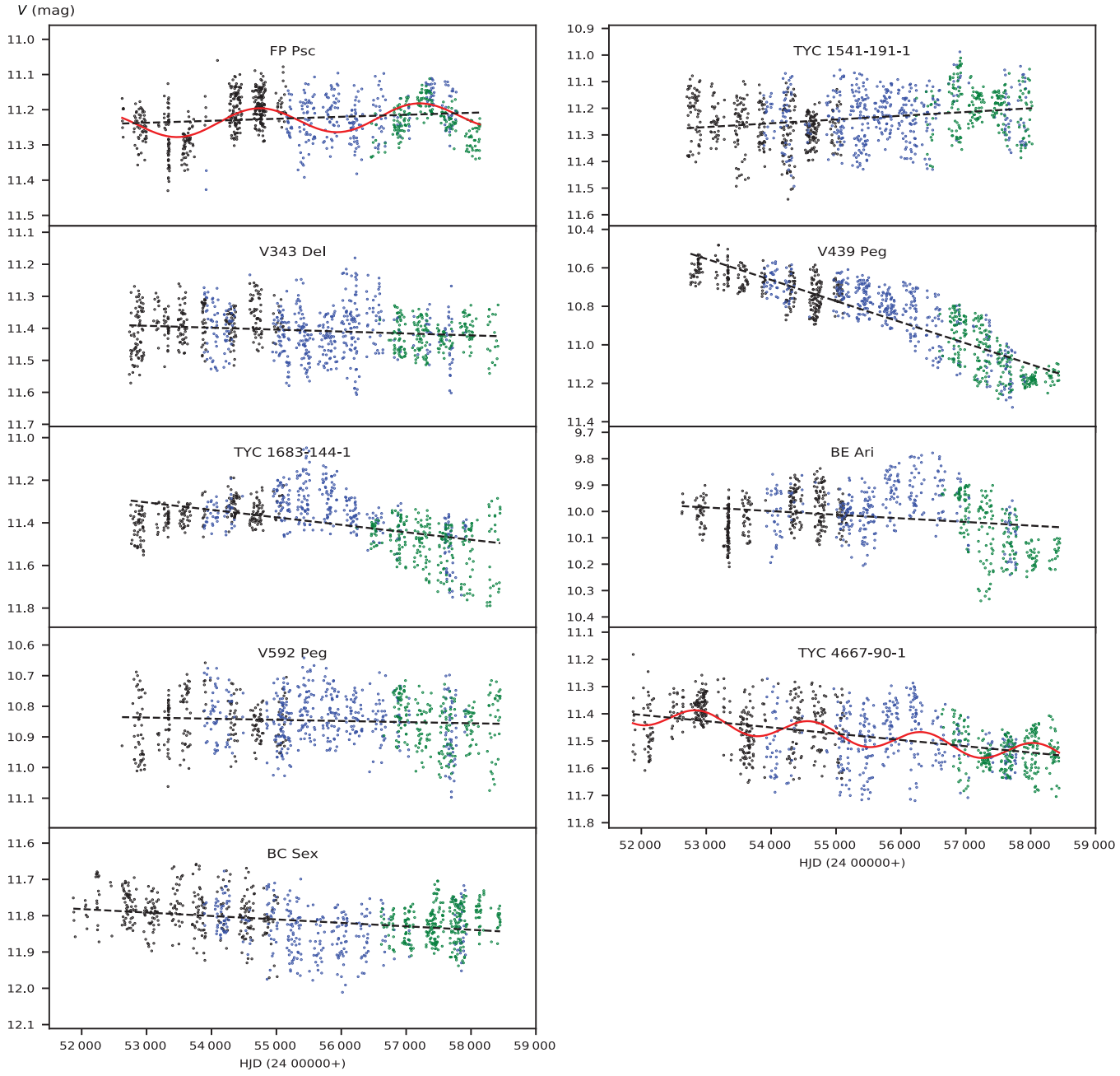

Figure 4. Continued.

much shorter rotation periods. In summary, photometric period continuously decreases through the cycle while light loss amplitude and mean brightness gradually increase in the first half of the cycle and then gradually decrease towards the end of the cycle.[3] At that point, we emphasise that the scenario outlined above does not strictly work through the cycle since sunspots could also be emerged at high or low latitudes in the middle of a sunspot cycle. However, these cases do not change the global trends observed in photometric properties.

[3]Note that the Sun appears brighter at the middle of a sunspot cycle due to the more dominant facular contribution to the brightness, compared to the spot contribution.

In order to evaluate each star in the context described above, we present seasonal behaviours of the mean V brightness, peak-to-peak light curve amplitude (A), and photometric period (P) of each target star in Figure 5. Although photometric data spans over 14–18 yr, one may notice some missing seasons in the figure. These missing seasons are due to the sparse data or very low light curve amplitude, which prevent us from finding reliable photometric period and light curve amplitude. Still, we inspect Figure 5, especially for stars exhibiting photometric cycles. For a given target with a cyclic mean brightness variation, general distribution of seasonal photometric periods does not appear coherent with the corresponding cycle and exhibits scattered pattern rather than a systematic decrease trend that repeats itself

https://doi.org/10.1017/pasa.2021.21 Published online by Cambridge University Press

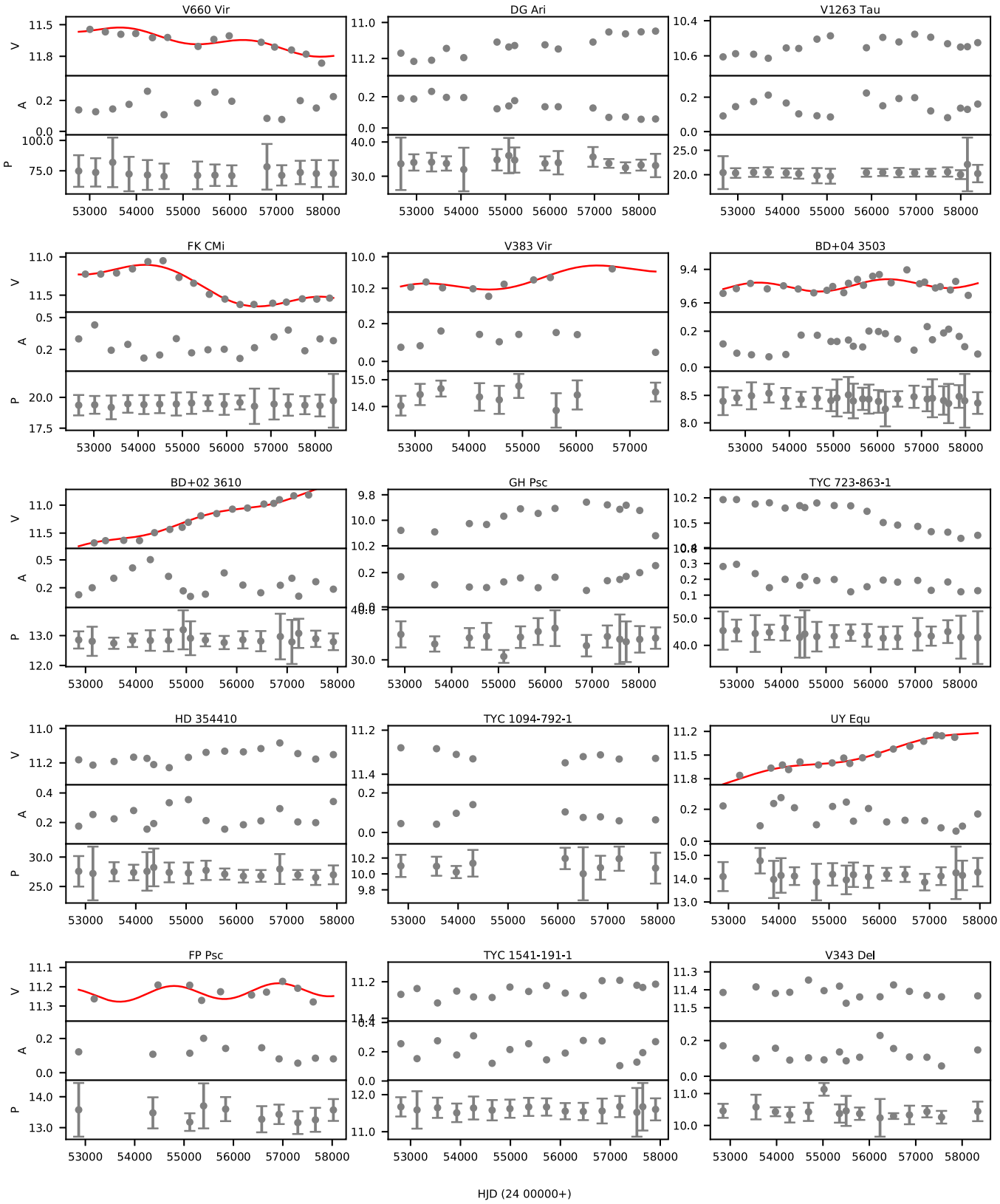

Figure 5. Seasonal mean brightness (*V*, mag), peak-to-peak light curve amplitude (*A*, mag), and photometric period (*P*, day) of each target star are plotted versus time. Detected long-period cycles are overplotted with red continuous line.

https://doi.org/10.1017/pasa.2021.21 Published online by Cambridge University Press

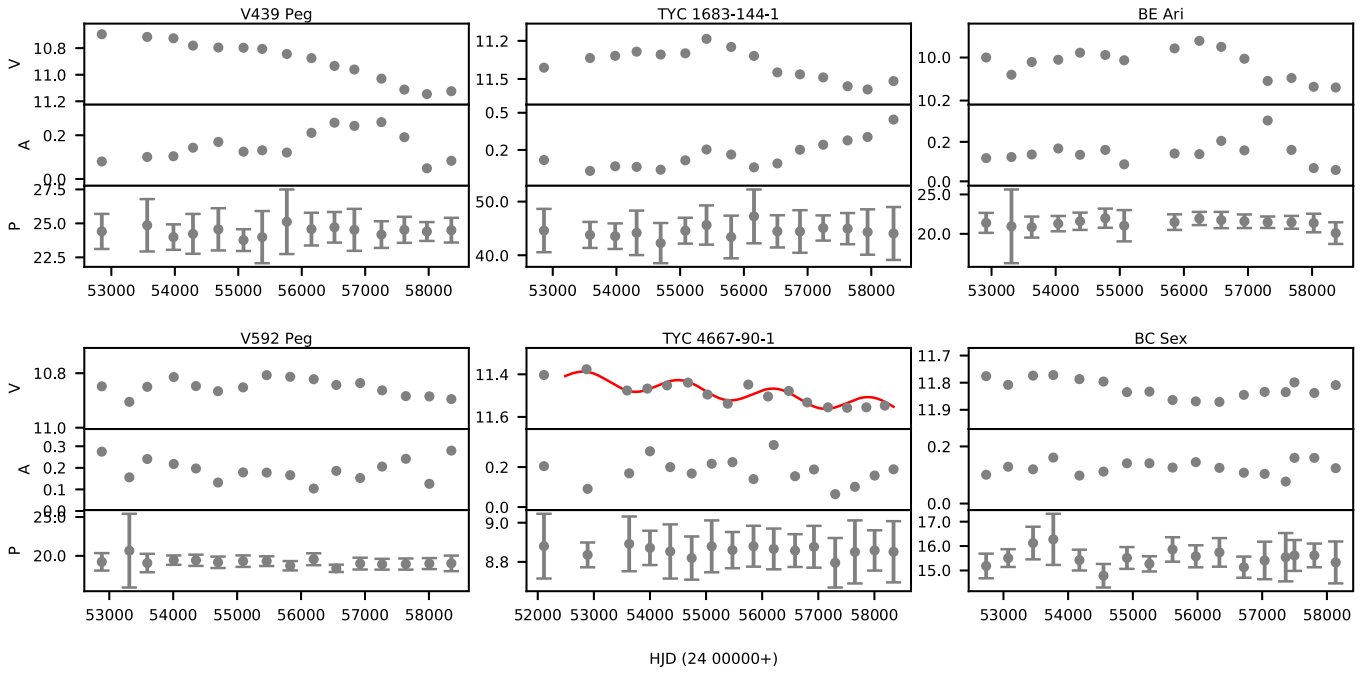

Figure 5. Continued.

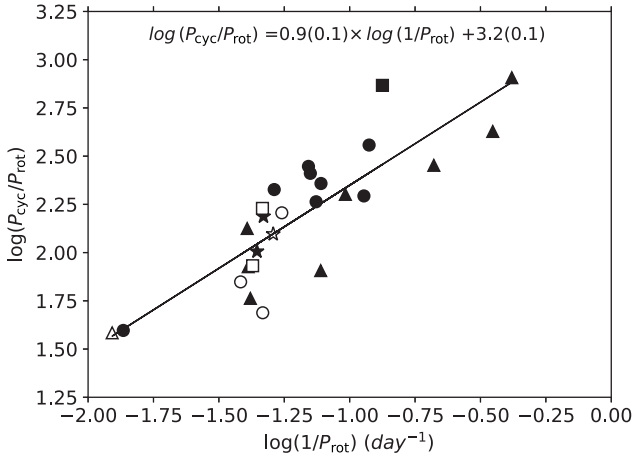

Figure 6. Relation between log $(1/P_{rot})$ and log (P_{cyc}/P_{rot}) for giant and subgiant stars. Filled circles are stars listed in Table 3, open circles show BD+13 5000, TYC 5163-1764-1 and BD+11 3024 (Özdarcan & Dal 2018), filled stars denote HD 208472 (Özdarcan et al. 2010) and HD 89546 (Özdarcan et al. 2012), filled triangles are for IM Peg, HK Lac, XX Tri, IL Hya, HU Vir, UZ Lib, V711 Tau, and FK Com (Oláh et al. 2009), open squares show IS Vir and V2253 Oph (Oláh et al. 2013) open triangle is BM Cam (Zboril & Messina 2009), filled square is DM UMa (Taş & Evren 2012), and open star is σ Gem (Kajatkari et al. 2014). Equation of the linear fit is indicated in the insert where numbers in parentheses show statistical errors for the last digit.

in each cycle as observed in the sunspot cycle. Regarding light curve amplitude and mean brightness, it is noticeable that the mean brightness tends to increase as the peak-to-peak light curve amplitude decreases.

4. Activity cycle length, rotation period, and relative surface shear

We plot target stars listed in Table 3 on $\log(1/P_{\rm rot}) - \log(P_{\rm cyc}/P_{\rm rot})$ plane in Figure 6, where $P_{\rm rot}$ is the rotation period in day. We also overplot same values of previously published giant or subgiant stars in the figure. We observe a clear linear trend as reported in previous studies (Baliunas et al. 1996; Oláh & Strassmeier 2002; Oláh et al. 2009, Suárez Mascareño, Rebolo, & González Hernández 2016); however, we provide quantitative representation of the trend by only using giant and subgiant stars. Linear representation of the data leads to the relation inserted in the figure with a correlation coefficient of 0.85 and probability of no correlation $p = 3.5 \times 10^{-8}$.

Using maximum and minimum photometric periods of each target tabulated in Table C.1, we compute relative surface shear of each target in terms of $\Delta P/P_{\rm min}$. Here, $\Delta P = P_{\rm max} - P_{\rm min}$, where $P_{\rm max}$ and $P_{\rm min}$ denote maximum and minimum periods, respectively. We plot logarithm of the relative surface shear $\log(\Delta P/P_{\rm min})$ versus $\log(P_{\rm min})$ in Figure 7 and we find another positive linear correlation with a correlation coefficient of 0.67 and probability of no correlation $p = 1.9 \times 10^{-4}$. We also overplot the main sequence stars studied by Donahue et al. (1996), who obtained results with a method similar to the one described in our study. Here, we note that we consider minimum periods tabulated in Table 1 of Donahue et al. (1996) study and compute $\Delta P/P_{\rm min}$ from these data in order to evaluate both datasets properly. Linear regression to the main sequence star data in Figure 7 gives a slope of 0.3, a correlation coefficient of 0.4, and probability of no correlation $p = 0.014$. One may easily observe the clear separation of two samples. For a given period, magnitude of the relative surface shear is clearly larger in main sequence stars than giant and subgiant stars. The correlation denotes that the relative surface shear increases with increasing rotational period. Although both samples show positive linear correlations, giant and subgiant sample exhibit linear trend with steeper slope and larger correlation coefficient than the main sequence sample.

We also inspect possible relation between the activity cycle length and the relative surface shear in Figure 8. Distribution of the data practically indicates no correlation between the cycle length and the relative surface shear.

https://doi.org/10.1017/pasa.2021.21 Published online by Cambridge University Press

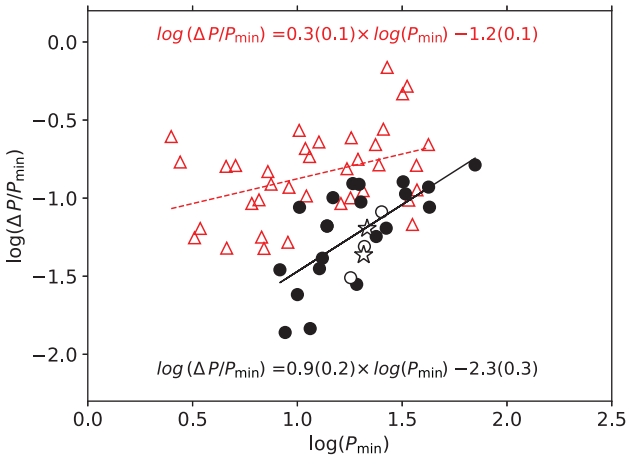

Figure 7. Relation between the minimum rotation period P_{min} and the relative surface shear $\Delta P/P_{min}$ on the logarithmic scale. Filled circles are stars listed in Table 3, open circles show BD+13 5000, TYC 5163-1764-1, and BD+11 3024 (Özdarcan & Dal 2018), open stars denote HD 208472 (Özdarcan et al. 2010) and HD 89546 (Özdarcan et al. 2012). Equation of the linear fit (black continuous line) is indicated in the insert (bottom). Open red triangles show stars taken from Donahue et al. (1996) and the linear representation of their distribution is shown by red dashed line and given in the insert (top).

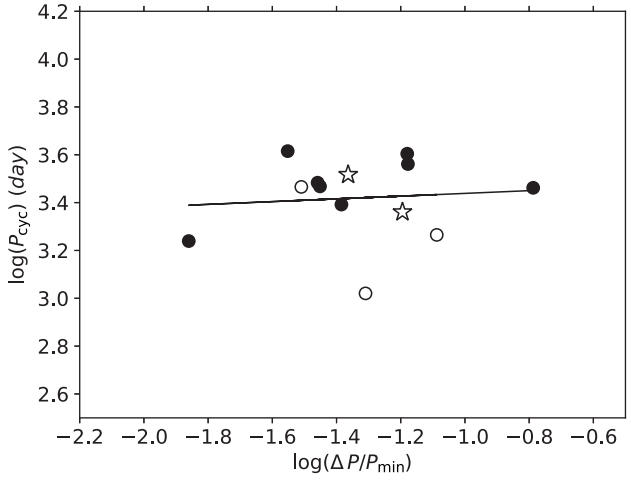

Figure 8. Relation between the activity cycle length and the relative surface shear on the logarithmic scale. The symbols have the same meaning as in Figure 7.

5. Summary and discussion

We present analysis of medium resolution optical spectra and long-term V-band photometry of 21 cool stars. All stars exhibit direct emission features in Ca II H& K line profiles, while we observe both filled emission and direct emission in H_α lines. Emission features in these spectral lines are clear evidences of chromospheric activity on the target stars. LTE spectrum synthesis shows that the target stars are cool red giant or subgiant stars with an overall metallicity, [M/H], between 0 and −0.5.

Analysis of long-term V-band photometry of target stars reveals that DG Ari, V1263 Tau, HD 354410, TYC 1541-191-1, V343 Del, and V592 Peg undergo linear mean brightness variation, which may indicate activity cycles in very long timescales. We detect single significant period for eight of the target stars, V660 Vir, FK CMi, V383 Vir, BD+04 3503, BD+02 3610, UY Equ, FP Psc, and TYC 4667-90-1. For each target, resulting cycle signal is superimposed on a linear brightening or dimming trend. Linear trend might show a part of a possible second cycle with a much longer timescale compared to the current dataset. In other words, these stars might possess multiple cycles. Remaining target stars appear to possess photometric cycles, but time base of the current data is not sufficient to confirm these cycles. Possible long-term cycles can be checked only with further V-band observations. Here, we also stress that the cycle periods found in our analysis may only be average values. In case of the sunspot cycle, one can only give an average 11 yr of period, which actually varies between 9 and 14 yr. Therefore, in the context of solar–stellar connection, it is not reasonable to accept strict period values in case of stellar magnetic activity cycles. Oláh, Kolláth, & Strassmeier (2000), and Oláh et al. (2009) clearly showed that photometric cycle periods of cool active stars are variable.

Further analysis of long-term photometric data in terms of seasonal light curve analysis yield photometric period, peak-to-peak light curve amplitude, minimum, maximum, and mean brightnesses of each observing season. For a given target, we compute average value of the seasonal photometric periods and adopt it as the photometric rotation period, P_{rot}, of the target. Then, we inspect the relation between $\log(1/P_{rot})$ and $\log(P_{cyc}/P_{rot})$ of giant and subgiant stars. We observe clear linear trend on the logarithmic scale with a slope of 0.9 ± 0.1, which is consistent with that derived by the slope reported by Oláh et al. (2009, 0.81 ± 0.05) within 1σ level but is considerably higher than the slope reported by Baliunas et al. (1996, 0.74), who originally tested the equivalency of the stellar dynamo number ($D \sim 1/P_{rot}$) and P_{cyc}/P_{rot} ratio. We note that our sample includes only giant and subgiant stars, while Oláh et al. (2009) used a homogeneous sample, including main sequence and giant stars. If we do not consider the giant stars taken from their study, the slope of the linear fit in Figure 6 increases to 1.0 ± 0.2. In any case, these slopes are considerably smaller than the one found in theoretical computations of Dubé & Charbonneau (2013, 1.47), who mentioned that the observed linear relation is the robust property of kinematic mean field $\alpha\Omega$ dynamo models with α quenching. Our results support this picture since the activity cycle length is weakly anti-correlated with the relative surface shear, indicating that the activity cycle should be mainly driven by turbulent diffusivity, rather than the differential rotation as anticipated in non-linearly saturated dynamo models. However, although activity cycle length does not appear sensitive to the rotation period for our sample (see Figure 6), longer period stars still tends to have longer period activity cycles, which contradicts with the prediction given by Dubé & Charbonneau (2013).

Assuming that the P_{min} corresponds to the equatorial rotation period, we find that the relative surface shear, $\Delta P/P_{min}$, is positively correlated with the equatorial rotation period, which means differential rotation tends to be stronger for slow rotators. Reinhold & Gizon (2015) made photometric analysis of 12 319 Kepler stars, which are homogeneously distributed in temperature and luminosity class and found that the positive correlation between P_{min} and the differential rotation exists for stars cooler than 6 000 K. At that point, our study provides quantitative description of the relation for cool giants and subgiant. Moreover, overplotting main sequence stars from the study of Donahue et al. (1996) in Figure 7, we observe the clear separation between two samples and more steep slope for giant and subgiant stars. The

https://doi.org/10.1017/pasa.2021.21 Published online by Cambridge University Press

separation becomes more remarkable towards the shorter periods. Considering evolutionary properties of two samples, we may conclude that the relative surface shear is more sensitive to the rotation period in giant and subgiant stars compared to the main sequence stars. However, magnitude of the relative surface shear for a given period is larger for main sequence stars than giant and subgiant stars. This observational finding appear contradictory to the theoretical model predictions given in Kitchatinov & Rüdiger (1999). On the other hand, Kövári et al. (2017) studied the rotation and the differential rotation relationship via a homogeneous sample in luminosity class whose differential rotation parameters were obtained from Doppler imaging studies. They find a correlation similar to the one shown in Figure 7 but also noticed a distinction between single and binary stars, where the relative surface shear in single stars shows stronger dependency on the rotation period compared to the close binaries. It could be speculated that the separation observed in Figure 7 might be partly caused by being single or binary star. Nevertheless, this needs to be checked by high-resolution spectroscopy for all stars plotted in the figure.

Further analyses of individual targets indicate that temporal behaviour of the photometric period does not appear analogous to solar cycle and we do not observe any significant relation between photometric period, mean brightness, and light curve amplitude. We can only say that the mean brightness generally tends to increase as the peak-to-peak light curve amplitude decreases. One may conclude that photometric cycle properties of target stars are not similar to the photometric properties of the sunspot cycle. However, as mentioned in Fekel et al. (2002), the observed photometric period could be affected by the growth and decay of spots or spot groups at various latitudes and longitudes, which means the observed photometric period may not be adopted as a true period of any stellar latitude. Therefore, observed temporal distributions of photometric periods in Figure 5 might partly originate from spot growth and decay. With the current data, it is not possible to arrive at a conclusive result. Further regular V band photometric observations should be continued for successive cycles, so that global photometric behaviour could show itself more clearly in longer timescales. That was the case for HD 89546, where 11 yr of observations did not yield any significant correlation between the photometric period and the mean brightness (Fekel et al. 2002), but doubling the time base of the photometric data yielded the correlation (Özdarcan et al. 2012). Another possibility is that the distribution of the photometric period might be related to a possible cycle which has a timescale longer than the current time base of the photometric data. Observed linear trends in the mean brightness of our target stars might indicate such longer-term cycles. Consequently, we may observe only a part of the whole photometric period variation pattern, which appears as a scatter.

Acknowledgements. I am indebted to Dr. Grzegorz Pojmański for reducing and providing unpublished ASAS-3N data, which compensate long data gap between published ASAS3 and ASAS-SN data and increase the precision of the main results of this study. I also express my thanks to Dr. Hasan Ali Dal for fruitful discussion on statistical analyses. I acknowledge the anonymous referee for his/her helpful comments and valuable suggestions that have significantly contributed to improve the paper. I further thank TÜBİTAK National Observatory for a partial support in using RTT150 (Russian-Turkish 1.5-m telescope in Antalya) with project numbers 14BRTT150-678 and 18BRTT150-1275. This research has made use of the SIMBAD database, operated at CDS, Strasbourg, France. This research received no specific grant from any funding agency, commercial, or not-for-profit sectors.

References

Alvarez, R., & Plez, B. 1998, A&A, 330, 1109
Baliunas, S. L., et al. 1995, ApJ, 438, 269
Baliunas, S. L., Nesme-Ribes, E., Sokoloff, D., & Soon, W. H. 1996, ApJ, 460, 848
Berdnikov, L. N., & Pastukhova, E. N. 2008, PZ, 28, 9
Bernhard, K. 2008, OEJV, 0078, 1
Bernhard, K., & Lloyd, C. 2008a, OEJV, 0082, 1
Bernhard, K., & Lloyd C. 2008b, OEJV, 0086, 1
Bernhard, K., & Lloyd C. 2008c, OEJV, 0089, 1
Bernhard, K., & Lloyd C. 2008d, OEJV, 0092, 1
Bernhard, K., & Otero, S. 2011, PZP, 11, 15
Blanco-Cuaresma, S., Soubiran, C., Heiter, U., & Jofré P. 2014, A&A, 569, A111
Bressan, A., Marigo, P., Girardi, L., Salasnich, B., Dal Cero, C., Rubele, S., & Nanni, A. 2012, MNRAS, 427, 127
Donahue, R. A., Saar, S. H., & Baliunas, S. L. 1996, ApJ, 466, 384
Dubé, C., & Charbonneau, P. 2013, ApJ, 775, 69
Duncan, D. K., et al. 1991, ApJS, 76, 383
Fekel, F. C., & Henry, G. W. 2005, AJ, 129, 1669
Fekel, F. C., Henry, G. W., Eaton, J. A., Sperauskas, J., & Hall, D. S. 2002, AJ, 124, 1064
Frasca, A., Covino, E., Spezzi, L., Alcalá, J. M., Marilli, E., FŻrÉsz, G., & Gandolfi, D. 2009, A&A, 508, 1313
Gray, D. F. 2005, The Observation and Analysis of Stellar Photospheres (3rd edn.; Cambridge University Press)
Gray, R. O., Corbally, C. J., Garrison, R. F., McFadden, M. T., & Robinson, P. E. 2003, AJ, 126, 2048
Gustafsson, B., Edvardsson, B., Eriksson, K., Jørgensen, U. G., Nordlund, Å., & Plez, B. 2008, A&A, 486, 951
Henry, G. W., & Eaton, J. A., ed. 1995, Robotic Telescopes: Current Capabilities, Present Developments, and Future Prospects for Automated Astronomy: Proceedings of a Symposium Held as Part of the 106th Annual Meeting of the Astronomical Society of the Pacific, Flagstaff, Arizona, 28–30 June 1994 Astronomical Society of the Pacific Conference Series, Vol. 79
Hickey, J. R., Alton, B. M., Kyle, H. L., & Hoyt, D. 1988, SSR, 48, 321
Høg, E., et al. 2000, A&A, 355, L27
Jetsu, L., Henry, G. W., & Lehtinen, J. 2017, ApJ, 838, 122
JofrÉ, E., Petrucci, R., Saffe, C., Saker, L., Artur de la Villarmois, E., Chavero, C., Gómez, M., & Mauas, P. J. D. 2015, A&A, 574, A50
Kajatkari, P., Hackman, T., Jetsu, L., Lehtinen, J., & Henry, G. W. 2014, A&A, 562, A107
Kiraga, M. 2012, A&A, 62, 67
Kitchatinov, L. L., & Rüdiger, G. 1999, A&A, 344, 911
Kochanek, C. S., et al. 2017, PASP, 129, 104502
Kövári, Z., Oláh, K., Kriskovics, L., Vida, K., Forgács-Dajka, E., & Strassmeier, K. G. 2017, AN, 338, 903
Lloyd, C., Schirmer, J., Bernhard, K., & Frank, P. 2011, OEJV, 136, 1
Lockwood, G. W., Skiff, B. A., & Radick, R. R. 1997, ApJ, 485, 789
Lomb, N. R. 1976, Ap&SS, 39, 447
Messina, S., & Guinan, E. F. 2003, A&A, 409, 1017
Oláh, K., et al. 2009, A&A, 501, 703
Oláh, K., Kolláth, Z., & Strassmeier, K. G. 2000, A&A, 356, 643
Oláh, K., Moór, A., Strassmeier, K. G., Borkovits, T., & Granzer, T. 2013, AN, 334, 625
Oláh K., Strassmeier K. G., 2002, AN, 323, 361
Özdarcan, O., & Dal, H. A. 2018, AN, 339, 277
Özdarcan, O., Evren, S., Strassmeier, K. G., Granzer, T., & Henry, G. W. 2010, AN, 331, 794
Özdarcan, O., Evren, S., & Henry, G. W. 2012, AN, 333, 138
Plez, B. 2012, Turbospectrum: Code for spectral synthesis (ascl:1205.004)
Pojmanski, G. 1997, A&A, 47, 467
Pojmanski, G. 2002, A&A, 52, 397
PojmaŃski, G. 2021, Priv
Pojmanski, G., Pilecki, B., & Szczygiel, D. 2005, A&A, 55, 275
Radick, R. R., Lockwood, G. W., Skiff, B. A., & Baliunas, S. L. 1998, ApJS, 118, 239

https://doi.org/10.1017/pasa.2021.21 Published online by Cambridge University Press

Reinhold, T., & Gizon, L. 2015, A&A, 583, A65
Rodonò, M., Cutispoto, G., Lanza, A. F., & Messina, S. 2001, AN, 322, 333
Ryabchikova, T., Piskunov, N., Kurucz, R. L., Stempels, H. C., Heiter, U., Pakhomov, Y., & Barklem, P. S. 2015, PhyS, 90, 054005
Scargle, J. D. 1982, ApJ, 263, 835
Schirmer, J., Bernhard, K., & Lloyd, C. 2009, OEJV, 105, 1
Schmidt, E. G., Hemen, B., Rogalla, D., & Thacker-Lynn, L. 2009, AJ, 137, 4598
Schwarzenberg-Czerny, A. 1991, MNRAS, 253, 198
Schwarzenberg-Czerny, A. 1996, ApJ, 460, L107
Shappee, B. J., et al. 2014, ApJ, 788, 48
Soubiran, C., Bienaymé, O., Mishenina, T. V., & Kovtyukh, V. V. 2008, A&A, 480, 91
Strassmeier, K. G., Boyd, L. J., Epand, D. H., & Granzer, T. 1997, PASP, 109, 697
Suárez Mascareño, A., Rebolo, R., & González Hernández, J. I. 2016, A&A, 595, A12
Taş, G., & Evren, S. 2012, BaltA, 21, 435
Vaughan, A. H., Preston, G. W., & Wilson, O. C. 1978, PASP, 90, 267
Wilson, O. C. 1978, ApJ, 226, 379
Zacharias, N., Finch, C. T., Girard, T. M., Henden, A., Bartlett, J. L., Monet, D. G., & Zacharias, M. I. 2013, AJ, 145, 44
Zboril, M., & Messina, S. 2009, AN, 330, 377

A. Observed and the best-fitting synthetic spectra

We present plots of observed and the best-fitting synthetic spectrum for each target star separately in Figure A.1.

B. Lomb–Scargle amplitude spectra

We present Lomb–Scargle amplitude spectra of the stars with cyclic mean brightness variation shown in Figure 4.

C. Seasonal photometric analysis of target stars

We tabulate seasonal photometric analysis results in Table C.1.

https://doi.org/10.1017/pasa.2021.21 Published online by Cambridge University Press

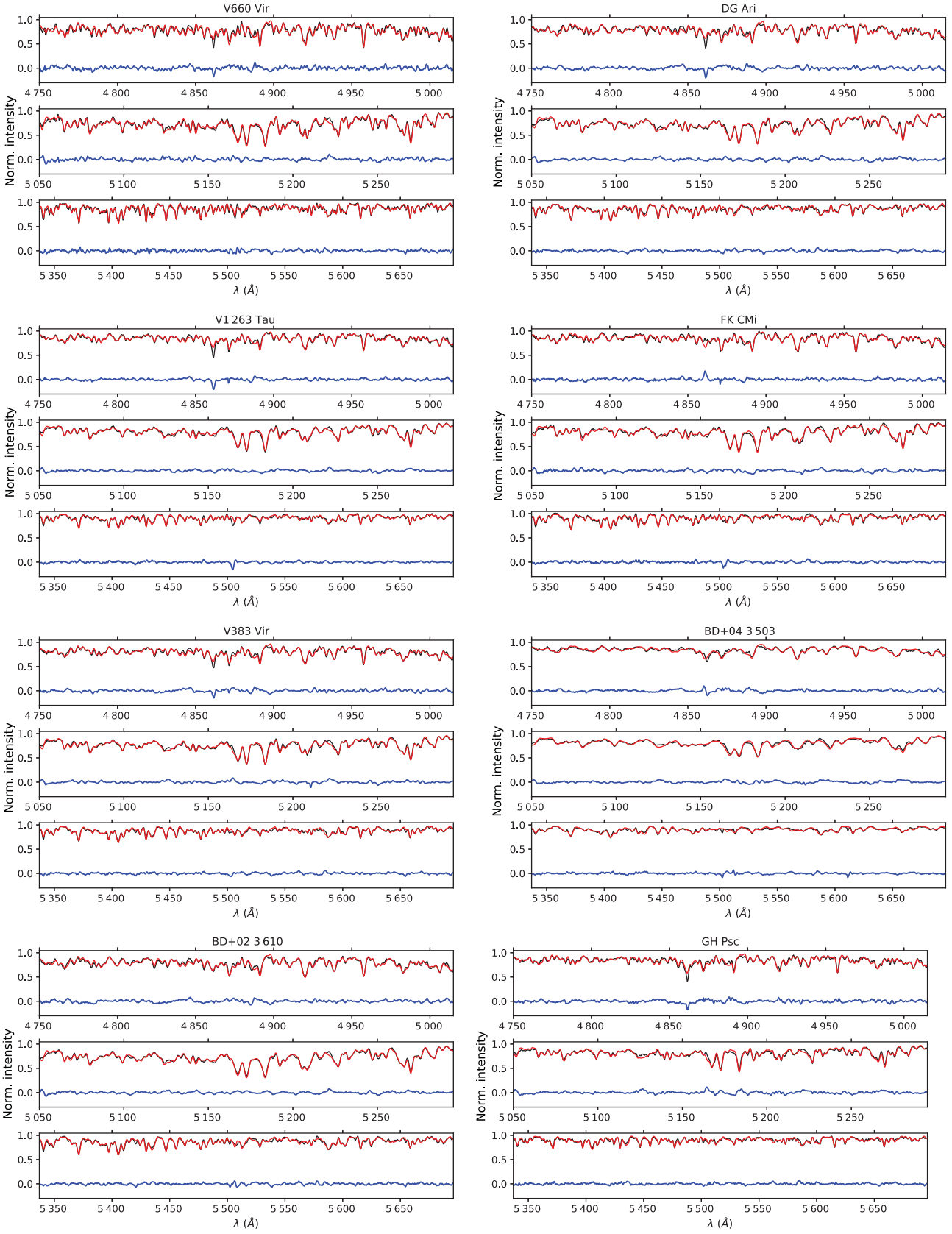

Figure A.1. Representative plots of atmospheric analysis results for target stars. Observed (black) and best-fitting (red) synthetic spectra together with residuals (blue) are shown for three regions in three windows one under the other.

https://doi.org/10.1017/pasa.2021.21 Published online by Cambridge University Press

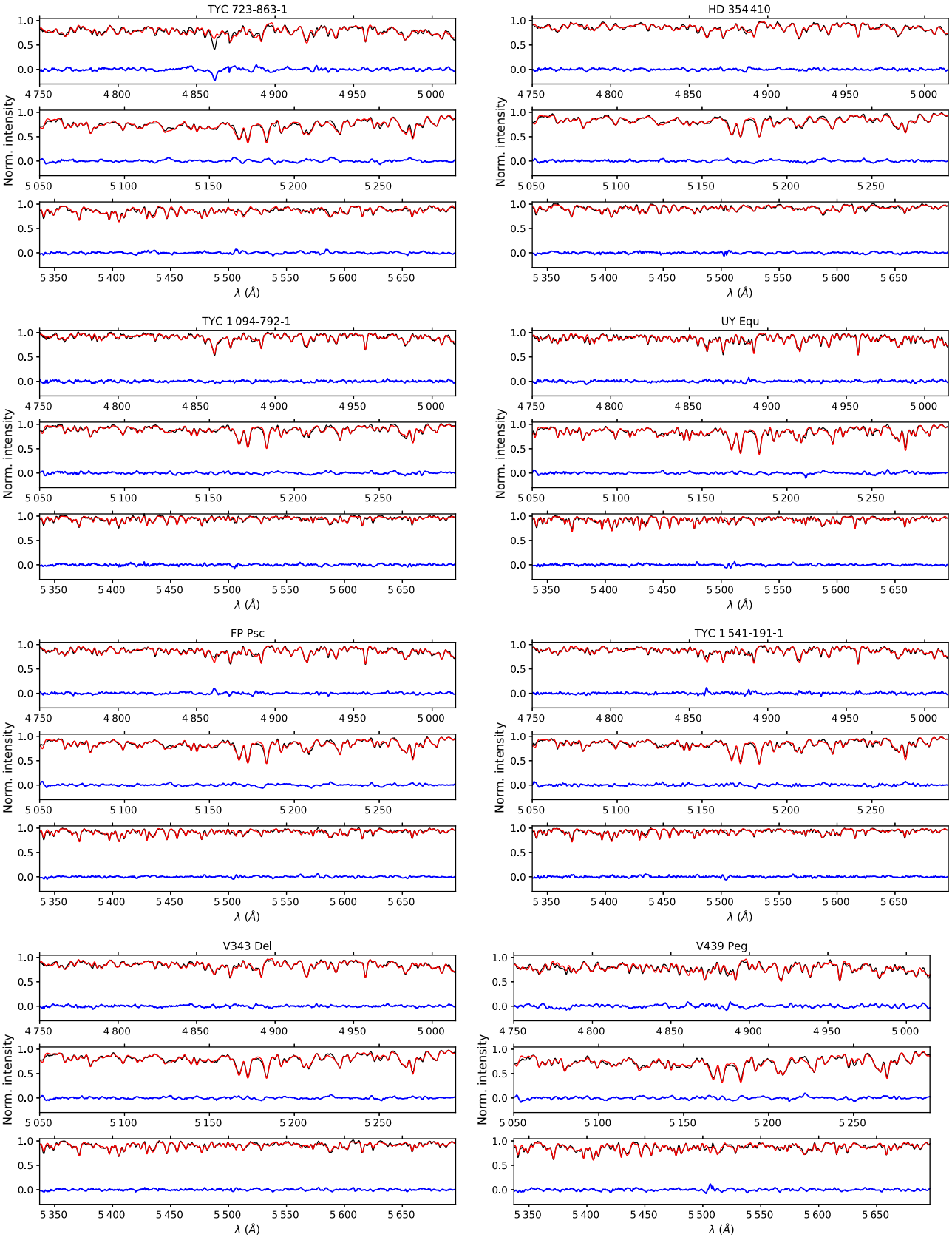

Figure A.1. Continued.

https://doi.org/10.1017/pasa.2021.21 Published online by Cambridge University Press

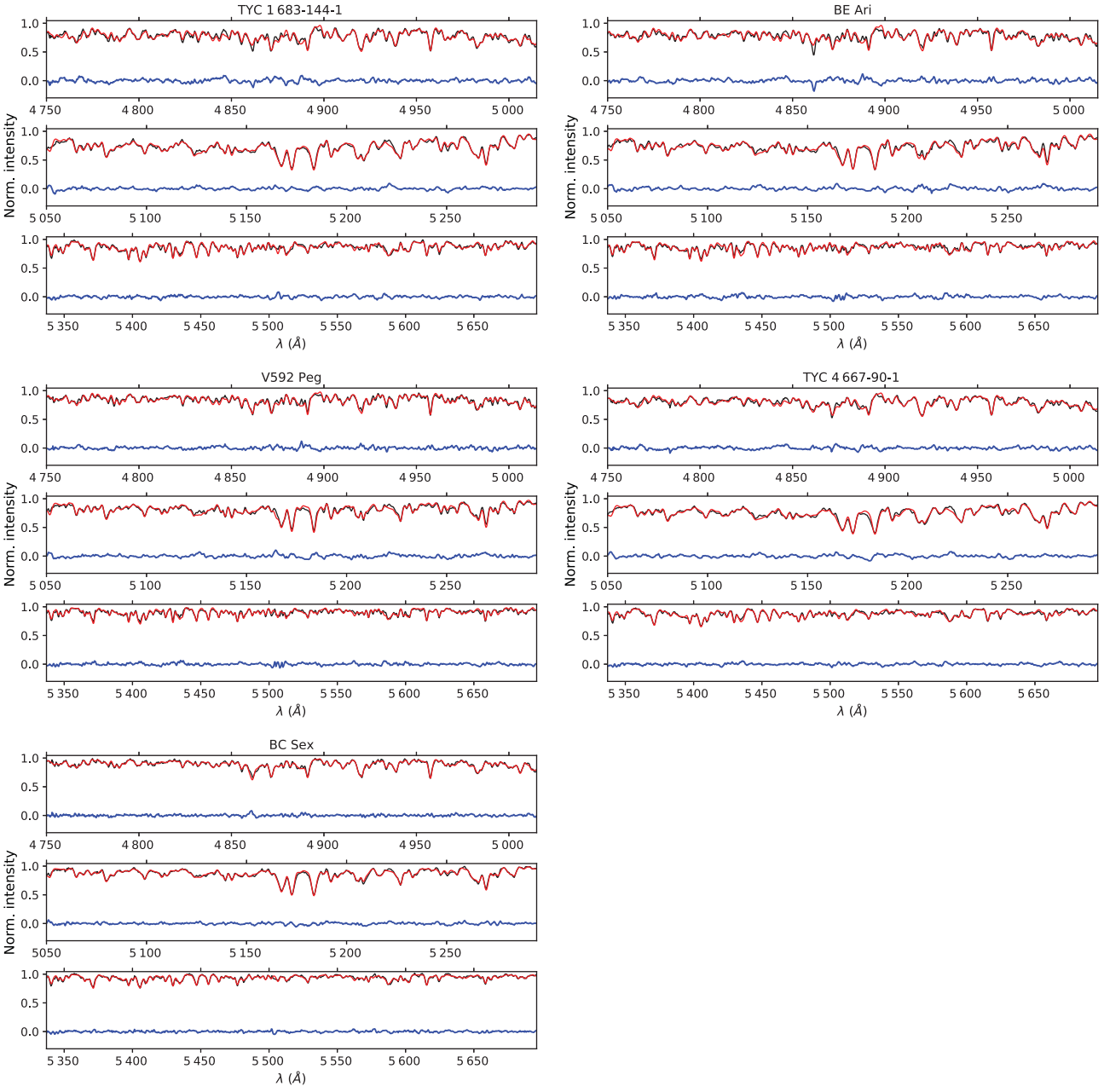

Figure A.1. Continued.

https://doi.org/10.1017/pasa.2021.21 Published online by Cambridge University Press

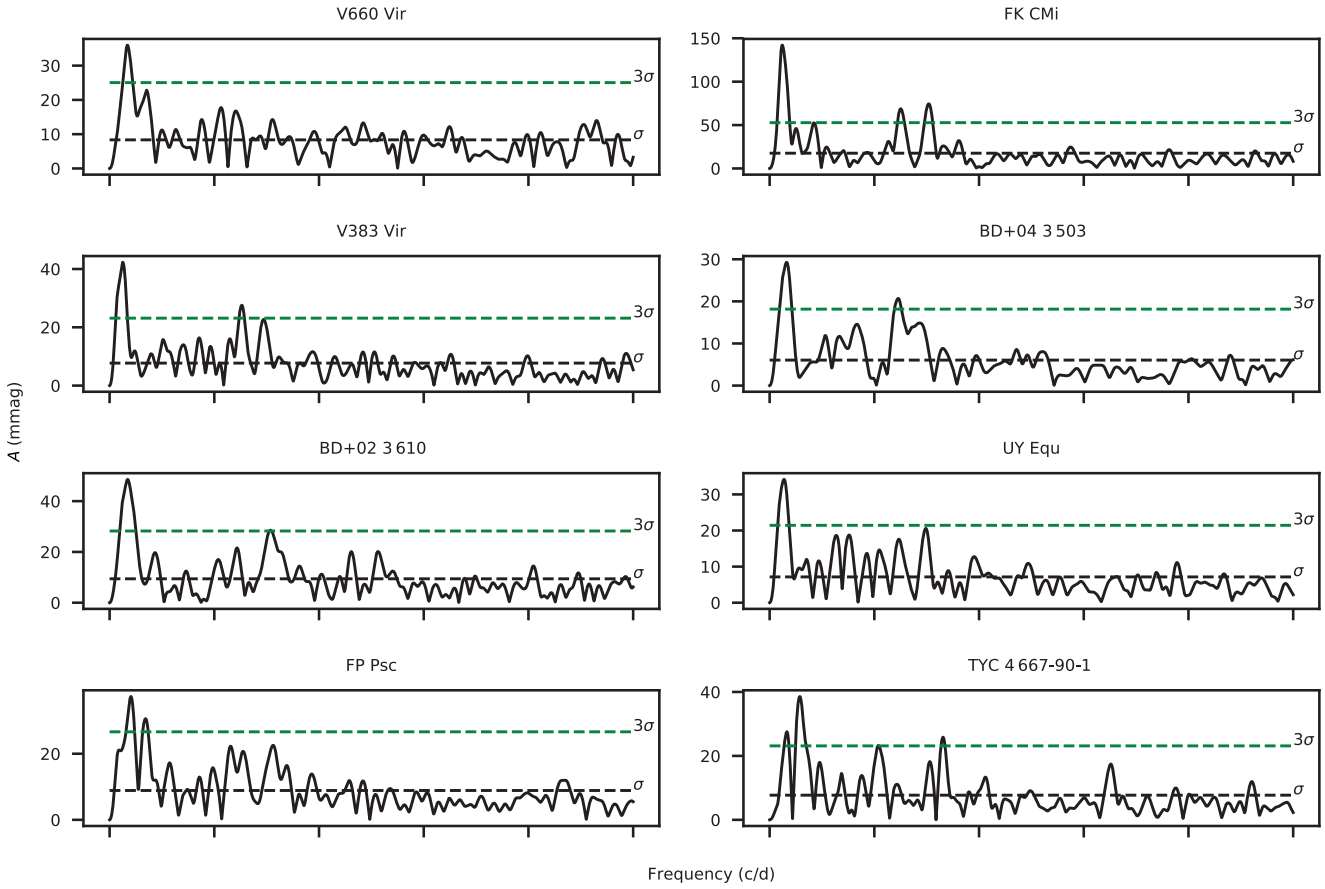

Figure B.1 Lomb–Scargle amplitude spectra of the stars with detected cycle frequencies. Horizontal dashed lines show 1σ and 3σ uncertainty levels. 1σ level is the mean of the amplitude spectrum, which is computed by excluding the dominant peak and its close vicinity.

https://doi.org/10.1017/pasa.2021.21 Published online by Cambridge University Press

Table C.1 Photometric analysis results of seasonal light curves. Columns are start, end, and mean HJD of the corresponding light curve, time span of the dataset (Δt), computed photometric period (P) and its uncertainty, maximum, minimum, and mean brightnesses, peak-to-peak amplitude of the light curve (A), and number of data points in the light curve (N). We list computed average photometric period (P_{rot}) of each target as two columns list at the end of the table. Uncertainty of P_{rot} is computed via standard deviation of seasonal photometric periods.

HJD start	HJD end	HJD mean	Δt (day)	P (day)	max (mag)	min (mag)	mean (mag)	A (mag)	N
V660 Vir									
52 652.8631	52 875.5046	52 764.1839	222.64	75 ± 13	11.468	11.607	11.537	0.139	58
53 036.8567	53 219.5272	53 128.1920	182.67	74 ± 12	11.494	11.621	11.557	0.127	28
53 396.8736	53 589.5255	53 493.1996	192.65	82 ± 20	11.504	11.649	11.576	0.145	46
53 754.8625	53 931.8480	53 843.3553	176.99	72 ± 14	11.482	11.657	11.570	0.175	30
54 136.8491	54 339.4810	54 238.1651	202.63	72 ± 12	11.473	11.733	11.603	0.260	70
54 480.1409	54 708.4795	54 594.3102	228.34	70 ± 11	11.547	11.655	11.601	0.108	50
55 176.1530	55 448.7186	55 312.4358	272.57	71 ± 11	11.580	11.763	11.672	0.183	80
55 567.1414	55 801.7374	55 684.4394	234.60	71 ± 9	11.489	11.743	11.616	0.254	41
55 926.1492	56 165.7471	56 045.9482	239.60	71 ± 9	11.491	11.686	11.588	0.195	49
56 740.8665	56 857.8001	56 799.3333	116.93	78 ± 19	11.597	11.681	11.639	0.084	24
56 992.1584	57 240.7435	57 116.4510	248.59	71 ± 8	11.639	11.716	11.677	0.077	66
57 386.1205	57 639.7231	57 512.9218	253.60	74 ± 10	11.601	11.800	11.700	0.199	73
57 752.1058	57 961.7584	57 856.9321	209.65	73 ± 11	11.658	11.809	11.733	0.151	56
58 120.1164	58 325.7653	58 222.9409	205.65	73 ± 11	11.691	11.916	11.804	0.225	26
DG Ari									
52 621.5762	52 674.5304	52 648.0533	52.95	34 ± 8	11.118	11.308	11.213	0.190	22
52 831.9138	53 046.5255	52 939.2197	214.61	34 ± 2	11.177	11.363	11.270	0.186	55
53 266.8093	53 410.5355	53 338.6724	143.73	34 ± 3	11.145	11.379	11.262	0.234	22
53 564.9302	53 779.5349	53 672.2326	214.60	34 ± 2	11.082	11.278	11.180	0.196	88
54 012.8949	54 111.6050	54 062.2500	98.71	32 ± 6	11.146	11.341	11.244	0.195	47
54 757.7669	54 861.7684	54 809.7677	104.00	35 ± 3	11.075	11.198	11.136	0.123	28
55 014.1144	55 135.7166	55 074.9155	121.60	36 ± 5	11.099	11.240	11.170	0.141	52
55 144.7181	55 268.7446	55 206.7314	124.03	35 ± 4	11.072	11.247	11.160	0.175	48
55 775.0789	56 000.7400	55 887.9095	225.66	34 ± 2	11.087	11.223	11.155	0.136	50
56 127.1154	56 246.0212	56 186.5683	118.91	34 ± 3	11.116	11.252	11.184	0.136	39
56 836.1130	57 098.7185	56 967.4158	262.61	36 ± 3	11.072	11.200	11.136	0.128	61
57 203.1194	57 444.7839	57 323.9517	241.66	34 ± 1	11.032	11.100	11.066	0.068	74
57 564.1174	57 831.7193	57 697.9184	267.60	33 ± 2	11.044	11.115	11.079	0.071	78
57 930.1178	58 167.5161	58 048.8170	237.40	33 ± 2	11.037	11.093	11.065	0.056	78
58 297.1116	58 450.9446	58 374.0281	153.83	33 ± 3	11.031	11.089	11.060	0.058	22
V1263 Tau									
52 627.5901	52 710.4978	52 669.0440	82.91	20.4 ± 3.4	10.561	10.652	10.606	0.091	27
52 831.9085	53 068.5029	52 950.2057	236.59	20.4 ± 1.0	10.516	10.661	10.588	0.145	57
53 269.7895	53 439.4971	53 354.6433	169.71	20.5 ± 0.9	10.504	10.678	10.591	0.174	28
53 564.9349	53 801.5031	53 683.2190	236.57	20.5 ± 1.0	10.508	10.720	10.614	0.212	47
53 987.0826	54 184.7266	54 085.9046	197.64	20.4 ± 0.9	10.472	10.638	10.555	0.166	45
54 293.9180	54 439.6196	54 366.7688	145.70	20.2 ± 1.0	10.507	10.610	10.558	0.103	48
54 725.8015	54 825.7000	54 775.7508	99.90	19.8 ± 1.6	10.459	10.551	10.505	0.092	45
55 021.9329	55 132.7437	55 077.3383	110.81	19.7 ± 1.5	10.443	10.528	10.486	0.085	38
55 763.1018	56 006.7237	55 884.9128	243.62	20.4 ± 0.9	10.442	10.666	10.554	0.224	40
56 144.1033	56 359.7326	56 251.9180	215.63	20.5 ± 0.7	10.420	10.570	10.495	0.150	36
56 527.0755	56 700.7722	56 613.9239	173.70	20.4 ± 1.0	10.425	10.617	10.521	0.192	24
56 865.1191	57 070.7448	56 967.9320	205.63	20.4 ± 0.8	10.378	10.575	10.477	0.197	59

https://doi.org/10.1017/pasa.2021.21 Published online by Cambridge University Press

Table C.1 Continued.

HJD start	HJD end	HJD mean	Δt (day)	P (day)	max (mag)	min (mag)	mean (mag)	A (mag)	N
V1263 Tau									
57 209.1200	57 444.7155	57 326.9178	235.60	20.4 ± 0.8	10.434	10.554	10.494	0.120	53
57 581.1132	57 829.7404	57 705.4268	248.63	20.6 ± 1.0	10.491	10.572	10.531	0.081	73
57 934.9328	58 056.6148	57 995.7738	121.68	20.0 ± 0.9	10.482	10.618	10.550	0.136	22
58 121.8736	58 179.5138	58 150.6937	57.64	22.1 ± 5.5	10.484	10.613	10.548	0.129	25
58 312.1149	58 451.8172	58 381.9661	139.70	20.2 ± 1.8	10.445	10.605	10.525	0.160	26
FK CMi									
52 519.9188	52 794.4482	52 657.1835	274.53	19.4 ± 0.8	11.059	11.392	11.225	0.333	67
52 894.9005	53 142.4838	53 018.6922	247.58	19.4 ± 0.7	11.004	11.446	11.225	0.442	73
53 271.8805	53 512.4605	53 392.1705	240.58	19.2 ± 1.0	11.089	11.333	11.211	0.244	50
53 650.8099	53 883.4558	53 767.1329	232.65	19.5 ± 0.7	11.012	11.302	11.157	0.290	62
54 014.1014	54 247.4538	54 130.7776	233.35	19.4 ± 0.8	10.971	11.154	11.062	0.183	98
54 365.8936	54 608.4666	54 487.1801	242.57	19.5 ± 0.7	10.946	11.153	11.050	0.207	81
54 755.8638	54 969.7379	54 862.8008	213.87	19.5 ± 0.9	11.102	11.437	11.269	0.335	63
55 080.1348	55 336.7457	55 208.4403	256.61	19.5 ± 0.9	11.232	11.456	11.344	0.224	85
55 449.1376	55 705.7368	55 577.4372	256.60	19.5 ± 0.6	11.365	11.613	11.489	0.248	66
55 825.1099	56 065.7458	55 945.4279	240.64	19.4 ± 0.8	11.425	11.677	11.551	0.252	82
56 185.1273	56 415.7740	56 300.4507	230.65	19.6 ± 0.6	11.532	11.712	11.622	0.180	73
56 575.1265	56 682.9616	56 629.0441	107.84	19.3 ± 1.4	11.489	11.753	11.621	0.264	30
57 009.8632	57 132.7543	57 071.3088	122.89	19.5 ± 1.3	11.431	11.779	11.605	0.348	111
57 285.0992	57 499.7415	57 392.4204	214.64	19.4 ± 0.9	11.390	11.792	11.591	0.402	143
57 639.1269	57 895.7541	57 767.4405	256.63	19.4 ± 0.7	11.428	11.668	11.548	0.240	137
57 997.1318	58 220.7822	58 108.9570	223.65	19.3 ± 0.9	11.386	11.719	11.552	0.333	101
58 372.1080	58 451.0433	58 411.5757	78.94	19.7 ± 2.2	11.380	11.699	11.539	0.319	19
V383 Vir									
52 623.8560	52 845.4759	52 734.6660	221.62	14.0 ± 0.4	10.156	10.231	10.193	0.075	76
52 996.8488	53 189.4938	53 093.1713	192.64	14.5 ± 0.4	10.118	10.201	10.160	0.083	40
53 387.8449	53 575.5043	53 481.6746	187.66	14.7 ± 0.3	10.116	10.277	10.197	0.161	26
54 079.1257	54 319.4656	54 199.2957	240.34	14.4 ± 0.5	10.132	10.275	10.203	0.143	68
54 461.8549	54 674.4738	54 568.1644	212.62	14.3 ± 0.5	10.199	10.303	10.251	0.104	54
54 822.8532	55 040.4717	54 931.6625	217.62	14.8 ± 0.5	10.103	10.246	10.174	0.143	40
55 572.1075	55 682.8917	55 627.4996	110.78	13.9 ± 0.6	10.071	10.224	10.147	0.153	22
55 951.0409	56 091.8590	56 021.4500	140.82	14.4 ± 0.5	10.061	10.203	10.132	0.142	36
57 357.0975	57 601.7468	57 479.4221	244.65	14.5 ± 0.4	10.053	10.101	10.077	0.048	78
BD+04 3503									
52 443.6524	52 548.5211	52 496.0868	104.87	8.4 ± 0.3	9.462	9.624	9.543	0.162	15
52 684.8874	52 933.4962	52 809.1918	248.61	8.5 ± 0.1	9.466	9.564	9.515	0.098	65
53 063.8970	53 219.5369	53 141.7170	155.64	8.5 ± 0.3	9.440	9.527	9.484	0.087	24
53 424.8957	53 650.4952	53 537.6954	225.60	8.5 ± 0.2	9.480	9.553	9.516	0.073	49
53 790.8911	54 051.6848	53 921.2880	260.79	8.5 ± 0.2	9.453	9.542	9.498	0.089	66
54 146.1528	54 389.4928	54 267.8228	243.34	8.4 ± 0.1	9.406	9.629	9.517	0.223	117
54 521.8919	54 748.5111	54 635.2015	226.62	8.5 ± 0.2	9.429	9.651	9.540	0.222	77
54 854.1616	55 033.8503	54 944.0060	179.69	8.4 ± 0.2	9.436	9.615	9.525	0.179	54
55 039.5863	55 123.7295	55 081.6579	84.14	8.5 ± 0.3	9.413	9.592	9.502	0.179	32
55 299.0881	55 383.9764	55 341.5323	84.89	8.5 ± 0.3	9.444	9.633	9.539	0.189	49
55 394.8460	55 509.6889	55 452.2675	114.84	8.4 ± 0.3	9.410	9.556	9.483	0.146	39
55 587.1747	55 742.9733	55 665.0740	155.80	8.4 ± 0.2	9.390	9.531	9.460	0.141	36
55 751.8823	55 861.7194	55 806.8008	109.84	8.4 ± 0.3	9.369	9.620	9.495	0.251	37

https://doi.org/10.1017/pasa.2021.21 Published online by Cambridge University Press

Table C.1 Continued.

HJD start	HJD end	HJD mean	Δt (day)	P (day)	max (mag)	min (mag)	mean (mag)	A (mag)	N
BD+04 3503									
55 952.1726	56 094.9465	56 023.5596	142.77	8.4 ± 0.2	9.317	9.565	9.441	0.248	40
56 122.9147	56 235.7049	56 179.3098	112.79	8.3 ± 0.3	9.314	9.547	9.431	0.233	33
56 329.1577	56 587.7029	56 458.4303	258.55	8.4 ± 0.1	9.382	9.578	9.480	0.196	40
56 735.0999	56 924.7395	56 829.9197	189.64	8.5 ± 0.2	9.344	9.463	9.403	0.119	55
57 061.1213	57 195.7524	57 128.4369	134.63	8.4 ± 0.2	9.345	9.627	9.486	0.282	60
57 197.9403	57 297.7091	57 247.8247	99.77	8.5 ± 0.4	9.381	9.572	9.476	0.191	32
57 452.1425	57 550.9560	57 501.5493	98.81	8.4 ± 0.3	9.392	9.630	9.511	0.238	34
57 560.9541	57 669.7154	57 615.3348	108.76	8.4 ± 0.4	9.371	9.635	9.503	0.264	46
57 781.1742	57 928.9587	57 855.0665	147.78	8.5 ± 0.2	9.416	9.630	9.523	0.214	61
57 939.8826	58 020.7502	57 980.3164	80.87	8.4 ± 0.5	9.400	9.543	9.472	0.143	22
58 180.0800	58 371.7721	58 275.9261	191.69	8.4 ± 0.2	9.509	9.601	9.555	0.092	25
BD+02 3610									
52 782.7903	52 946.5080	52 864.6492	163.72	12.9 ± 0.3	11.582	11.769	11.676	0.187	39
53 072.8968	53 191.8071	53 132.3520	118.91	12.8 ± 0.5	11.511	11.761	11.636	0.250	21
53 444.8895	53 676.5003	53 560.6949	231.61	12.7 ± 0.2	11.463	11.798	11.630	0.335	61
53 802.8904	54 063.6839	53 933.2872	260.79	12.8 ± 0.2	11.421	11.849	11.635	0.428	46
54 163.1574	54 408.5049	54 285.8312	245.35	12.8 ± 0.3	11.242	11.744	11.493	0.502	108
54 525.1493	54 768.5136	54 646.8315	243.36	12.8 ± 0.4	11.259	11.611	11.435	0.352	82
54 881.1589	54 995.0737	54 938.1163	113.91	13.2 ± 0.7	11.286	11.508	11.397	0.222	27
55 006.7315	55 157.6880	55 082.2098	150.96	12.9 ± 0.6	11.222	11.394	11.308	0.172	43
55 240.1646	55 516.7072	55 378.4359	276.54	12.9 ± 0.2	11.095	11.287	11.191	0.192	60
55 622.1460	55 879.7065	55 750.9263	257.56	12.8 ± 0.2	10.961	11.344	11.152	0.383	54
56 001.1171	56 242.6934	56 121.9053	241.58	12.9 ± 0.3	10.935	11.209	11.072	0.274	58
56 360.1333	56 593.7143	56 476.9238	233.58	12.8 ± 0.3	10.949	11.154	11.052	0.205	24
56 811.0196	56 918.7944	56 864.9070	107.77	13.0 ± 0.8	10.845	11.117	10.981	0.272	22
57 050.1689	57 138.9662	57 094.5676	88.80	12.8 ± 0.7	10.801	11.136	10.969	0.335	22
57 153.9284	57 305.7317	57 229.8301	151.80	13.1 ± 0.5	10.816	10.990	10.903	0.174	24
57 420.1672	57 716.6892	57 568.4282	296.52	12.9 ± 0.3	10.681	10.985	10.833	0.304	48
57 797.1520	58 037.7156	57 917.4338	240.56	12.8 ± 0.3	10.700	10.937	10.819	0.237	59
GH Psc									
52 805.9188	53 025.5382	52 915.7285	219.62	35 ± 3	9.991	10.167	10.079	0.176	54
53 526.9347	53 750.5566	53 638.7457	223.62	33 ± 2	10.027	10.156	10.091	0.129	50
54 270.1107	54 487.7640	54 378.9374	217.65	34 ± 2	9.968	10.084	10.026	0.116	68
54 628.9285	54 864.7175	54 746.8230	235.79	35 ± 3	9.977	10.090	10.033	0.113	59
55 352.1168	55 589.7614	55 470.9391	237.64	35 ± 2	9.825	9.994	9.910	0.169	42
55 724.1049	55 973.7182	55 848.9116	249.61	36 ± 3	9.890	10.002	9.946	0.112	40
56 088.1099	56 329.7400	56 208.9250	241.63	36 ± 4	9.821	9.994	9.907	0.173	36
56 817.0922	56 944.0005	56 880.5464	126.91	33 ± 2	9.810	9.906	9.858	0.096	51
57 216.1141	57 437.7178	57 326.9160	221.60	35 ± 2	9.802	9.955	9.879	0.153	78
57 543.1121	57 643.8466	57 593.4794	100.73	34 ± 5	9.834	9.994	9.914	0.160	40
57 651.0251	57 806.7136	57 728.8694	155.69	34 ± 4	9.793	9.971	9.882	0.178	63
57 898.1166	58 139.5280	58 018.8223	241.41	34 ± 3	9.823	10.023	9.923	0.200	84
58 262.1160	58 451.7263	58 356.9212	189.61	34 ± 2	9.871	10.112	9.991	0.241	26

https://doi.org/10.1017/pasa.2021.21 Published online by Cambridge University Press

Table C.1 Continued.

HJD start	HJD end	HJD mean	Δt (day)	P (day)	max (mag)	min (mag)	mean (mag)	A (mag)	N
TYC 723-863-1									
52 621.7101	52 760.4668	52 691.0885	138.76	45 ± 7	10.127	10.408	10.268	0.281	91
52 861.9243	53 124.4644	52 993.1944	262.54	46 ± 4	10.119	10.414	10.267	0.295	88
53 355.6615	53 468.4951	53 412.0783	112.83	44 ± 7	10.193	10.429	10.311	0.236	27
53 622.9095	53 837.4799	53 730.1947	214.57	45 ± 3	10.226	10.373	10.299	0.147	36
53 990.1016	54 174.5673	54 082.3345	184.47	46 ± 5	10.251	10.451	10.351	0.200	52
54 350.9041	54 469.7513	54 410.3277	118.85	43 ± 7	10.246	10.408	10.327	0.162	21
54 473.6784	54 574.4688	54 524.0736	100.79	44 ± 9	10.238	10.454	10.346	0.216	31
54 722.8901	54 864.8412	54 793.8657	141.95	43 ± 5	10.205	10.397	10.301	0.192	33
55 068.1145	55 299.7702	55 183.9424	231.66	43 ± 4	10.227	10.426	10.326	0.199	55
55 425.1286	55 681.7392	55 553.4339	256.61	45 ± 3	10.269	10.390	10.329	0.121	51
55 793.1263	56 045.7432	55 919.4348	252.62	44 ± 4	10.307	10.460	10.383	0.153	43
56 156.1197	56 406.7659	56 281.4428	250.65	43 ± 4	10.396	10.591	10.494	0.195	39
56 526.1118	56 683.9819	56 605.0469	157.87	43 ± 4	10.428	10.610	10.519	0.182	22
57 008.9183	57 103.7544	57 056.3363	94.84	44 ± 6	10.436	10.629	10.532	0.193	29
57 238.1231	57 478.7392	57 358.4312	240.62	43 ± 4	10.519	10.649	10.584	0.130	70
57 653.0341	57 807.8102	57 730.4221	154.78	45 ± 4	10.497	10.680	10.589	0.183	70
57 969.1217	58 078.0550	58 023.5884	108.93	43 ± 8	10.589	10.710	10.650	0.121	27
58 352.1009	58 450.9988	58 401.5499	98.90	43 ± 10	10.556	10.684	10.620	0.128	16
HD 354410									
52 786.8037	52 942.5143	52 864.6590	155.71	27.6 ± 2.6	11.095	11.270	11.182	0.175	40
53 104.9163	53 190.7298	53 147.8231	85.81	27.2 ± 4.6	11.086	11.340	11.213	0.254	19
53 457.9060	53 678.5017	53 568.2039	220.60	27.5 ± 1.6	11.080	11.305	11.192	0.225	57
53 820.9129	54 093.6917	53 957.3023	272.78	27.4 ± 1.3	11.026	11.307	11.167	0.281	77
54 168.1427	54 277.9904	54 223.0666	109.85	27.6 ± 3.3	11.097	11.252	11.174	0.155	53
54 303.7262	54 409.5079	54 356.6171	105.78	28.2 ± 3.2	11.114	11.307	11.210	0.193	74
54 557.9038	54 772.5136	54 665.2087	214.61	27.4 ± 1.7	11.061	11.395	11.228	0.334	104
54 918.1385	55 175.6952	55 046.9169	257.56	27.3 ± 1.8	10.991	11.346	11.168	0.355	49
55 257.1488	55 537.7094	55 397.4291	280.56	27.7 ± 1.6	11.032	11.245	11.139	0.213	72
55 634.1418	55 902.6993	55 768.4206	268.56	27.1 ± 1.0	11.054	11.209	11.132	0.155	57
56 002.1209	56 277.6948	56 139.9079	275.57	26.8 ± 1.1	11.044	11.229	11.136	0.185	59
56 355.1490	56 621.7399	56 488.4445	266.59	26.8 ± 1.0	11.011	11.222	11.117	0.211	37
56 811.0726	56 917.8574	56 864.4650	106.78	28.0 ± 2.5	10.937	11.231	11.084	0.294	20
57 078.1607	57 366.7209	57 222.4408	288.56	27.0 ± 0.8	11.044	11.248	11.146	0.204	61
57 445.1627	57 710.7036	57 577.9332	265.54	26.5 ± 1.3	11.079	11.278	11.178	0.199	84
57 809.1644	58 049.7140	57 929.4392	240.55	27.0 ± 1.6	10.981	11.323	11.152	0.342	62
TYC 1094-792-1									
52 734.9017	52 970.5151	52 852.7084	235.61	10.1 ± 0.2	11.258	11.303	11.280	0.045	49
53 465.8989	53 669.5626	53 567.7308	203.66	10.1 ± 0.2	11.263	11.305	11.284	0.042	40
53 832.9117	54 093.6894	53 963.3006	260.78	10.0 ± 0.1	11.262	11.359	11.310	0.097	39
54 185.1482	54 408.5302	54 296.8392	223.38	10.2 ± 0.2	11.260	11.401	11.330	0.141	75
56 017.1221	56 275.7274	56 146.4248	258.61	10.2 ± 0.2	11.296	11.400	11.348	0.104	50
56 444.0241	56 571.8938	56 507.9590	127.87	10.0 ± 0.4	11.282	11.358	11.320	0.076	39
56 736.1416	56 971.7450	56 853.9433	235.60	10.1 ± 0.2	11.273	11.352	11.312	0.079	43
57 101.1487	57 357.6901	57 229.4194	256.54	10.2 ± 0.2	11.302	11.361	11.331	0.059	42
57 880.0301	58 037.8425	57 958.9363	157.81	10.1 ± 0.2	11.296	11.360	11.328	0.064	30

https://doi.org/10.1017/pasa.2021.21 Published online by Cambridge University Press

Table C.1 Continued.

HJD start	HJD end	HJD mean	Δt (day)	P (day)	max (mag)	min (mag)	mean (mag)	A (mag)	N
UY Equ									
52 812.9033	52 970.5311	52 891.7172	157.63	14.1 ± 0.6	11.576	11.852	11.714	0.276	43
53 554.7984	53 703.5227	53 629.1606	148.72	14.8 ± 0.6	11.577	11.698	11.637	0.121	30
53 850.9113	53 947.0851	53 898.9982	96.17	14.0 ± 0.8	11.456	11.751	11.604	0.295	26
53 986.8655	54 102.6934	54 044.7795	115.83	14.1 ± 0.7	11.483	11.824	11.653	0.341	25
54 197.1305	54 427.5313	54 312.3309	230.40	14.1 ± 0.4	11.441	11.703	11.572	0.262	68
54 696.7944	54 801.5217	54 749.1581	104.73	13.9 ± 0.8	11.539	11.668	11.604	0.129	24
54 949.9167	55 190.7242	55 070.3204	240.81	14.2 ± 0.5	11.446	11.718	11.582	0.272	65
55 285.1447	55 402.0050	55 343.5749	116.86	14.0 ± 0.6	11.378	11.684	11.531	0.306	23
55 406.9854	55 563.7050	55 485.3452	156.72	14.2 ± 0.5	11.510	11.667	11.589	0.157	36
55 657.1283	55 912.7219	55 784.9251	255.59	14.1 ± 0.5	11.400	11.656	11.528	0.256	49
56 018.1407	56 275.7333	56 146.9370	257.59	14.2 ± 0.3	11.417	11.568	11.492	0.151	47
56 381.1346	56 641.7071	56 511.4209	260.57	14.2 ± 0.3	11.354	11.518	11.436	0.164	40
56 812.0131	56 993.6882	56 902.8507	181.68	13.9 ± 0.4	11.327	11.487	11.407	0.160	60
57 101.1485	57 353.6942	57 227.4214	252.55	14.1 ± 0.4	11.302	11.407	11.354	0.105	43
57 464.1512	57 586.9492	57 525.5502	122.80	14.3 ± 1.1	11.251	11.330	11.290	0.079	24
57 591.9558	57 715.7601	57 653.8580	123.80	14.1 ± 0.6	11.237	11.355	11.296	0.118	45
57 879.0927	58 036.8399	57 957.9663	157.75	14.3 ± 0.6	11.205	11.418	11.312	0.213	36
FP Psc									
52 805.9122	52 924.7198	52 865.3160	118.81	13.6 ± 0.9	11.202	11.324	11.263	0.122	28
54 268.9217	54 467.5377	54 368.2297	198.62	13.5 ± 0.5	11.137	11.245	11.191	0.108	105
54 992.9334	55 238.7291	55 115.8313	245.80	13.2 ± 0.3	11.135	11.249	11.192	0.114	46
55 334.1201	55 457.9180	55 396.0191	123.80	13.7 ± 0.7	11.170	11.371	11.271	0.201	26
55 721.1098	55 962.7415	55 841.9257	241.63	13.6 ± 0.4	11.155	11.297	11.226	0.142	47
56 795.1118	57 054.7536	56 924.9327	259.64	13.4 ± 0.3	11.188	11.269	11.228	0.081	75
57 169.1114	57 439.7144	57 304.4129	270.60	13.2 ± 0.4	11.144	11.200	11.172	0.056	76
57 533.1165	57 788.7498	57 660.9332	255.63	13.3 ± 0.4	11.165	11.250	11.208	0.085	68
57 914.0927	58 135.7146	58 024.9037	221.62	13.6 ± 0.4	11.238	11.319	11.279	0.081	41
TYC 1541-191-1									
52 701.8917	52 911.5072	52 806.6995	209.62	11.7 ± 0.3	11.142	11.397	11.269	0.255	60
53 070.8966	53 189.6945	53 130.2956	118.80	11.6 ± 0.5	11.160	11.313	11.237	0.153	32
53 431.8987	53 649.4923	53 540.6955	217.59	11.7 ± 0.3	11.178	11.453	11.316	0.275	58
53 798.8989	54 051.6875	53 925.2932	252.79	11.5 ± 0.3	11.162	11.340	11.251	0.178	58
54 139.1229	54 384.4883	54 261.8056	245.37	11.6 ± 0.3	11.128	11.437	11.283	0.309	106
54 524.1304	54 743.4964	54 633.8134	219.37	11.6 ± 0.3	11.225	11.346	11.286	0.121	97
54 853.1692	55 126.7551	54 989.9622	273.59	11.6 ± 0.3	11.122	11.337	11.229	0.215	81
55 221.1609	55 509.6987	55 365.4298	288.54	11.7 ± 0.2	11.125	11.380	11.253	0.255	86
55 586.1656	55 860.7450	55 723.4553	274.58	11.7 ± 0.2	11.149	11.294	11.221	0.145	66
55 951.1618	56 243.6924	56 097.4271	292.53	11.6 ± 0.2	11.166	11.357	11.262	0.191	71
56 320.1500	56 597.7231	56 458.9366	277.57	11.6 ± 0.2	11.138	11.415	11.276	0.277	50
56 731.0462	56 940.7133	56 835.8798	209.67	11.6 ± 0.3	11.057	11.331	11.194	0.274	70
57 096.0361	57 283.7574	57 189.8968	187.72	11.7 ± 0.3	11.140	11.245	11.192	0.105	45
57 478.1151	57 585.7944	57 531.9548	107.68	11.5 ± 0.7	11.154	11.283	11.219	0.129	27
57 595.9300	57 703.6909	57 649.8105	107.76	11.7 ± 0.6	11.134	11.328	11.231	0.194	38
57 790.1326	58 021.7369	57 905.9348	231.60	11.6 ± 0.3	11.079	11.348	11.213	0.269	59

https://doi.org/10.1017/pasa.2021.21 Published online by Cambridge University Press

Table C.1 Continued.

HJD start	HJD end	HJD mean	Δt (day)	P (day)	max (mag)	min (mag)	mean (mag)	A (mag)	N
V343 Del									
52 734.9157	52 956.5249	52 845.7203	221.61	10.5 ± 0.2	11.308	11.521	11.415	0.213	72
53 481.9100	53 630.5173	53 556.2137	148.61	10.6 ± 0.4	11.321	11.447	11.384	0.126	48
53 848.9124	54 101.7168	53 975.3146	252.80	10.4 ± 0.1	11.322	11.518	11.420	0.196	73
54 191.1360	54 376.5014	54 283.8187	185.37	10.3 ± 0.2	11.358	11.471	11.414	0.113	74
54 590.9162	54 785.5172	54 688.2167	194.60	10.4 ± 0.3	11.282	11.411	11.346	0.129	55
54 942.1224	55 103.8006	55 022.9615	161.68	11.1 ± 0.2	11.347	11.462	11.405	0.115	49
55 283.1300	55 429.8992	55 356.5146	146.77	10.4 ± 0.3	11.295	11.465	11.380	0.170	40
55 432.9555	55 566.7074	55 499.8315	133.75	10.5 ± 0.5	11.421	11.529	11.475	0.108	31
55 647.1297	55 934.7009	55 790.9153	287.57	10.4 ± 0.2	11.373	11.506	11.440	0.133	63
56 182.8956	56 277.7237	56 230.3097	94.83	10.2 ± 0.6	11.297	11.582	11.439	0.285	38
56 391.1256	56 652.7378	56 521.9317	261.61	10.3 ± 0.1	11.276	11.470	11.373	0.194	37
56 736.1241	56 993.6943	56 864.9092	257.57	10.3 ± 0.3	11.342	11.477	11.409	0.135	64
57 098.1498	57 385.7052	57 241.9275	287.56	10.4 ± 0.2	11.364	11.497	11.431	0.133	76
57 481.1227	57 630.9719	57 556.0473	149.85	10.3 ± 0.2	11.403	11.475	11.439	0.072	35
58 257.0335	58 416.8097	58 336.9216	159.78	10.4 ± 0.3	11.342	11.526	11.434	0.184	19
V439 Peg									
52 755.9110	52 942.5388	52 849.2249	186.63	24.4 ± 1.3	10.569	10.669	10.619	0.100	42
53 487.9188	53 641.5124	53 564.7156	153.59	24.9 ± 1.9	10.581	10.707	10.644	0.126	31
53 853.9200	54 102.7015	53 978.3108	248.78	24.0 ± 0.9	10.592	10.722	10.657	0.130	47
54 196.1349	54 376.5014	54 286.3182	180.37	24.2 ± 1.5	10.636	10.815	10.726	0.179	59
54 590.9162	54 780.5525	54 685.7344	189.64	24.6 ± 1.6	10.638	10.850	10.744	0.212	88
54 962.1149	55 202.7004	55 082.4077	240.59	23.8 ± 0.8	10.668	10.824	10.746	0.156	72
55 305.1252	55 448.8158	55 376.9705	143.69	24.0 ± 1.9	10.675	10.839	10.757	0.164	40
55 701.0627	55 828.9585	55 765.0106	127.90	25.1 ± 2.4	10.730	10.881	10.805	0.151	32
56 030.1217	56 275.7648	56 152.9433	245.64	24.6 ± 1.2	10.712	10.976	10.844	0.264	49
56 390.1337	56 641.7129	56 515.9233	251.58	24.7 ± 1.1	10.756	11.078	10.917	0.322	40
56 737.1496	56 920.8622	56 829.0059	183.71	24.5 ± 1.5	10.799	11.103	10.951	0.304	67
57 115.1390	57 395.7062	57 255.4226	280.57	24.2 ± 1.0	10.875	11.200	11.037	0.325	87
57 475.1370	57 758.7495	57 616.9433	283.61	24.5 ± 1.0	11.020	11.259	11.140	0.239	82
57 847.1342	58 097.6999	57 972.4171	250.57	24.4 ± 0.7	11.152	11.213	11.182	0.061	51
58 279.9735	58 434.7789	58 357.3762	154.81	24.5 ± 0.9	11.103	11.207	11.155	0.104	19
TYC 1683-144-1									
52 754.9243	52 970.5297	52 862.7270	215.61	45 ± 4	11.335	11.517	11.426	0.182	53
53 492.9222	53 677.5650	53 585.2436	184.64	44 ± 2	11.309	11.418	11.363	0.109	34
53 858.9205	54 101.7196	53 980.3201	242.80	44 ± 2	11.278	11.418	11.348	0.140	39
54 202.1361	54 431.5198	54 316.8280	229.38	44 ± 4	11.253	11.389	11.321	0.136	66
54 588.9153	54 799.5226	54 694.2190	210.61	42 ± 4	11.281	11.398	11.340	0.117	54
54 952.9212	55 209.7027	55 081.3120	256.78	45 ± 2	11.242	11.422	11.332	0.180	61
55 310.1261	55 517.8448	55 413.9855	207.72	46 ± 4	11.110	11.363	11.237	0.253	57
55 667.1203	55 933.7198	55 800.4201	266.60	43 ± 4	11.180	11.399	11.290	0.219	54
56 046.1086	56 271.7605	56 158.9346	225.65	47 ± 5	11.282	11.415	11.349	0.133	44
56 399.1256	56 652.7506	56 525.9381	253.63	44 ± 3	11.377	11.536	11.457	0.159	47
56 751.1355	57 009.7120	56 880.4238	258.58	44 ± 4	11.344	11.595	11.470	0.251	65
57 121.1351	57 368.7044	57 244.9198	247.57	45 ± 2	11.348	11.633	11.490	0.285	56
57 488.1251	57 767.6997	57 627.9124	279.57	45 ± 3	11.391	11.705	11.548	0.314	93
57 848.1386	58 034.9142	57 941.5264	186.78	44 ± 4	11.400	11.737	11.569	0.337	44
58 248.0784	58 449.7614	58 348.9199	201.68	44 ± 5	11.287	11.741	11.514	0.454	28

https://doi.org/10.1017/pasa.2021.21 Published online by Cambridge University Press

Table C.1 Continued.

HJD start	HJD end	HJD mean	Δt (day)	P (day)	max (mag)	min (mag)	mean (mag)	A (mag)	N
BE Ari									
52 831.9007	53 000.5544	52 916.2276	168.65	21.4 ± 1.3	9.926	10.073	10.000	0.147	37
53 266.7132	53 354.6418	53 310.6775	87.93	21.0 ± 4.7	10.023	10.177	10.100	0.154	79
53 554.9116	53 699.5273	53 627.2195	144.62	20.9 ± 1.3	9.941	10.111	10.026	0.170	35
53 913.9295	54 166.7206	54 040.3251	252.79	21.3 ± 1.0	9.909	10.117	10.013	0.208	33
54 271.1014	54 489.8264	54 380.4639	218.72	21.6 ± 1.1	9.888	10.056	9.972	0.168	77
54 663.9351	54 884.7191	54 774.3271	220.78	22.0 ± 1.2	9.886	10.085	9.985	0.199	79
55 007.1005	55 131.6675	55 069.3840	124.57	21.0 ± 2.0	9.962	10.070	10.016	0.108	48
55 724.1090	55 985.7271	55 854.9181	261.62	21.5 ± 1.0	9.859	10.035	9.947	0.176	45
56 126.1039	56 356.7273	56 241.4156	230.62	22.0 ± 0.8	9.817	9.989	9.903	0.172	35
56 488.1031	56 677.7954	56 582.9493	189.69	21.8 ± 1.0	9.810	10.066	9.938	0.256	29
56 833.0949	57 054.7311	56 943.9130	221.64	21.6 ± 0.9	9.909	10.105	10.007	0.196	67
57 191.1148	57 422.7285	57 306.9217	231.61	21.5 ± 0.7	9.944	10.329	10.136	0.385	58
57 553.1079	57 804.7285	57 678.9182	251.62	21.5 ± 0.8	10.020	10.219	10.119	0.199	71
57 928.0916	58 121.8363	58 024.9640	193.74	21.4 ± 1.2	10.128	10.212	10.170	0.084	30
58 289.0944	58 447.7326	58 368.4135	158.64	20.1 ± 1.4	10.138	10.210	10.174	0.072	18
V592 Peg									
52 787.9299	52 976.5345	52 882.2322	188.60	19.2 ± 1.1	10.710	10.985	10.848	0.275	46
53 272.6082	53 353.5646	53 313.0864	80.96	20.7 ± 4.8	10.827	10.983	10.905	0.156	34
53 511.9307	53 675.5056	53 593.7182	163.57	19.1 ± 1.2	10.729	10.970	10.850	0.241	38
53 880.9290	54 134.7053	54 007.8172	253.78	19.5 ± 0.6	10.705	10.923	10.814	0.218	47
54 220.1181	54 490.7304	54 355.4243	270.61	19.4 ± 0.7	10.748	10.945	10.847	0.197	51
54 603.9285	54 797.5385	54 700.7335	193.61	19.2 ± 0.7	10.800	10.932	10.866	0.132	42
54 953.1182	55 232.7076	55 092.9129	279.59	19.3 ± 0.7	10.762	10.941	10.852	0.179	111
55 330.1191	55 593.7228	55 461.9210	263.60	19.3 ± 0.6	10.718	10.896	10.807	0.178	58
55 696.1255	55 963.7089	55 829.9172	267.58	18.7 ± 0.6	10.730	10.896	10.813	0.166	58
56 066.1185	56 329.7081	56 197.9133	263.59	19.6 ± 0.8	10.770	10.874	10.822	0.104	46
56 414.1215	56 688.7092	56 551.4154	274.59	18.4 ± 0.5	10.750	10.936	10.843	0.186	37
56 798.0969	57 050.7364	56 924.4167	252.64	19.0 ± 0.8	10.760	10.913	10.836	0.153	80
57 145.1190	57 390.7003	57 267.9097	245.58	18.9 ± 0.7	10.760	10.966	10.863	0.206	45
57 505.1261	57 772.6998	57 638.9130	267.57	18.9 ± 0.7	10.763	11.005	10.884	0.242	103
57 896.1224	58 117.7036	58 006.9130	221.58	19.0 ± 0.7	10.822	10.948	10.885	0.126	38
58 252.1053	58 449.8110	58 350.9582	197.71	19.0 ± 1.0	10.755	11.035	10.895	0.280	35
TYC 4667-90-1									
52 031.9292	52 190.6035	52 111.2664	158.67	8.9 ± 0.2	11.275	11.531	11.403	0.256	38
52 765.9179	53 012.5664	52 889.2422	246.65	8.8 ± 0.1	11.319	11.433	11.376	0.114	91
53 522.9048	53 736.5667	53 629.7358	213.66	8.9 ± 0.2	11.371	11.582	11.476	0.211	83
53 862.9236	54 137.7083	54 000.3160	274.78	8.8 ± 0.1	11.292	11.641	11.467	0.349	42
54 239.1160	54 482.7609	54 360.9385	243.64	8.8 ± 0.2	11.327	11.577	11.452	0.250	59
54 623.9319	54 863.7084	54 743.8202	239.78	8.8 ± 0.1	11.334	11.544	11.439	0.210	49
54 966.1240	55 233.7120	55 099.9180	267.59	8.9 ± 0.2	11.359	11.630	11.495	0.271	77
55 344.1096	55 595.7140	55 469.9118	251.60	8.8 ± 0.1	11.398	11.679	11.538	0.281	58
55 722.0833	55 968.7161	55 845.3997	246.63	8.9 ± 0.1	11.360	11.535	11.448	0.175	52
56 083.0915	56 328.7117	56 205.9016	245.62	8.8 ± 0.1	11.310	11.698	11.504	0.388	49
56 488.0529	56 682.7164	56 585.3847	194.66	8.8 ± 0.1	11.381	11.574	11.478	0.193	29
56 796.1160	57 048.7155	56 922.4158	252.60	8.9 ± 0.1	11.415	11.650	11.532	0.235	61
57 181.1062	57 420.7214	57 300.9138	239.62	8.7 ± 0.2	11.514	11.595	11.555	0.081	65

https://doi.org/10.1017/pasa.2021.21 Published online by Cambridge University Press

Table C.1 Continued.

HJD start	HJD end	HJD mean	Δt (day)	P (day)	max (mag)	min (mag)	mean (mag)	A (mag)	N
57 529.8962	57 774.7437	57 652.3200	244.85	8.8 ± 0.2	11.493	11.620	11.557	0.127	95
57 879.9202	58 126.6982	58 003.3092	246.78	8.8 ± 0.1	11.457	11.654	11.555	0.197	74
58 243.9249	58 436.7386	58 340.3318	192.81	8.8 ± 0.2	11.429	11.665	11.547	0.236	36
BC Sex									
52 622.8090	52 842.4570	52 732.6330	219.65	15.2 ± 0.5	11.725	11.826	11.776	0.101	58
52 958.8601	53 186.4881	53 072.6741	227.63	15.5 ± 0.4	11.744	11.873	11.808	0.129	50
53 356.8180	53 558.4726	53 457.6453	201.65	16.1 ± 0.7	11.714	11.834	11.774	0.120	33
53 703.8386	53 837.5961	53 770.7174	133.76	16.3 ± 1.1	11.692	11.853	11.772	0.161	29
54 058.0990	54 290.4657	54 174.2824	232.37	15.4 ± 0.4	11.738	11.836	11.787	0.098	70
54 430.8514	54 661.4638	54 546.1576	230.61	14.8 ± 0.5	11.740	11.852	11.796	0.112	65
54 794.8573	55 023.4622	54 909.1598	228.60	15.5 ± 0.5	11.765	11.906	11.835	0.141	58
55 129.1368	55 383.7457	55 256.4413	254.61	15.3 ± 0.3	11.763	11.904	11.833	0.141	59
55 487.1453	55 740.7607	55 613.9530	253.62	15.9 ± 0.5	11.801	11.927	11.864	0.126	30
55 855.1484	56 091.7872	55 973.4678	236.64	15.6 ± 0.5	11.797	11.942	11.869	0.145	44
56 233.1393	56 443.8411	56 338.4902	210.70	15.7 ± 0.6	11.808	11.933	11.871	0.125	31
56 615.0657	56 817.7909	56 716.4283	202.73	15.1 ± 0.4	11.791	11.899	11.845	0.108	40
56 943.1292	57 131.8679	57 037.4986	188.74	15.4 ± 0.8	11.782	11.886	11.834	0.104	52
57 309.1376	57 417.8940	57 363.5158	108.76	15.5 ± 1.0	11.796	11.873	11.835	0.077	41
57 420.7789	57 576.4712	57 498.6251	155.69	15.6 ± 0.6	11.719	11.879	11.799	0.160	55
57 672.1433	57 939.4703	57 805.8068	267.33	15.6 ± 0.5	11.758	11.918	11.838	0.160	127
58 074.8597	58 197.9610	58 136.4104	123.10	15.3 ± 0.9	11.747	11.871	11.809	0.124	29

Identifier	P_{rot} (day)
V660 Vir	73±3
DG Ari	34±1
V1263 Tau	20.4±0.5
FK CMi	19.4±0.1
V383 Vir	14.4±0.3
BD+04 3503	8.4±0.1
BD+02 3610	12.9±0.1
GH Psc	34.4±0.9
TYC 723-863-1	44±1
HD 354410	27.3±0.5
TYC 1094-792-1	10.1±0.1
UY Equ	14.1±0.2
FP Psc	13.4±0.2
TYC 1541-191-1	11.6±0.1
V343 Del	10.4±0.2
V439 Peg	24.4±0.4
TYC 1683-144-1	44±1
BE Ari	21.4±0.5
V592 Peg	19.2±0.5
TYC 4667-90-1	8.8±0.0
BC Sex	15.5±0.4

https://doi.org/10.1017/pasa.2021.21 Published online by Cambridge University Press